Metalliferous sediments from the H.M.S. *Challenger* voyage (1872–1876)

Vesselin M. Dekov [a,*], Javier Cuadros [b], George D. Kamenov [c], Dominik Weiss [d], Tim Arnold [d,e], Chandranath Basak [c], Pierre Rochette [f]

[a] *Department of Geology and Paleontology, University of Sofia, 15 Tzar Osvoboditel Blvd., 1000 Sofia, Bulgaria*
[b] *Department of Mineralogy, Natural History Museum, Cromwell Road, London SW7 5BD, UK*
[c] *Department of Geological Sciences, University of Florida, 241 Williamson Hall, Gainesville, FL 32611, USA*
[d] *Department of Earth Science and Engineering, Imperial College, Prince Consort Road, London SW7 2BP, UK*
[e] *Scripps Institution of Oceanography, University of California, San Diego, La Jolla, CA 92093, USA*
[f] *CEREGE, CNRS Université d'Aix-Marseille 3, Europole de l'Arbois BP80, 13545 Aix en Provence Cedex 4, France*

Abstract

The legendary cruise of H.M.S. *Challenger* (1872–1876) around the globe must always occupy an eminent place in the annals of oceanography, as being the first systematic attempt made on a global scale to explore the ocean. This expedition made fundamental discoveries in biology and geology which have not been surpassed by any later scientific cruise. Sediment with high content of metals (later called "metalliferous") was among the enigmatic findings taken onboard. Although the nature of metalliferous sediments is well known today, the very first sampled sediments of this type have not been studied to date. Motivated by the historical value of *Challenger*'s metalliferous sediment collection we undertook an investigation addressing two questions: (1) the composition of sediments from seafloor for which we have very limited data; (2) Sr–Nd–Pb–Fe–Zn-isotope signature of these sediments collected before the substantial human impact on the ocean during the 20th century.

The SE Pacific metalliferous sediments sampled by the *Challenger*'s explorers are of 2 types: (1) metalliferous oozes blanketing ridge crests and flanks down to the calcite compensation depth (CCD); and (2) stripped of $CaCO_3$ metalliferous sediments located beneath the CCD in the deeps near the mid-ocean ridges. The abiogenic part of these sediments is composed mainly of poorly-crystalline to X-ray amorphous Fe–Mn-oxyhydroxides, and an amorphous silicate phase. These sediments have geochemical features similar to those of all the other metalliferous sediments: very high Fe and Mn content (on abiogenic basis), very low Al/(Al + Fe + Mn), and high content (on abiogenic basis) of As, Ba, Be, Bi, Cd, Co, Cu, Mo, Ni, Pb, Sb, Th, Tl, U, V, W, Y, Zn and Zr. Their REE distribution patterns are similar to that of deep seawater and show weak signs of hydrothermal imprint (weak positive or no Eu anomaly).

Seawater and/or terrigenous input from South America control the Sr–Nd–Pb-isotope signature of the *Challenger* metalliferous sediments and have almost completely obliterated any original MORB-derived hydrothermal signal. Zn isotopes are mainly contributed from seawater although other Zn sources (hydrothermal fluid and detrital aluminosilicates, barite and volcanic glass) are necessary to fully explain Zn-isotope ratios. Fe isotopes indicate relatively slow Fe^{2+} to Fe^{3+} oxidation in the non-buoyant plume, thus producing relatively lighter Fe-isotope signature of the FeOOH particles that formed the studied metalliferous sediments.
© 2010 Elsevier Ltd. All rights reserved.

1. INTRODUCTION

The expedition of H.M.S. *Challenger* (1872–1876) inspired a new science, Oceanography, and became a major

landmark in its development. It could be argued that the discoveries of the cruise were one of the greatest advances in the knowledge of our planet since the renowned discoveries of the 15th and 16th centuries. Sediment with extremely high Fe and Mn content was among the discoveries of this expedition. Little attention was paid to this finding for the following 100 years until the discovery of seafloor hydrothermal vents (Corliss et al., 1979) awoke the scientific interest in this type of sediment. Metalliferous (hydrothermal) sediments are considered to be a result of either (1) hydrothermal non-buoyant plume fallout of Fe- and Mn-oxyhydroxide precipitates (distal sediments), or (2) mass-wasting and erosion of primary submarine massive sulfides, and hydrothermal buoyant plume fallout of Fe- and Mn-oxyhydroxides and sulfides (proximal sediments) (Mills and Elderfield, 1995; German and Von Damm, 2006; Rona, 2008). Many of the works on the metalliferous sediments (Boström, 1973; Bonatti, 1981; Hannington and Jonasson, 1992; Gurvich, 2006, and many others) refer to the Challenger's finding although the samples collected in this expedition have not been studied since that time. All we know about this unusual finding is contained in the Challenger report: a detailed sample description and chemical analyses for eight elements (Murray and Renard, 1891).

After the great excitement during the late 1960s–mid 1980s the interest in metalliferous sediments decreased. Scientists focused on the seafloor vent fluids, hydrothermal plumes, massive hydrothermal deposits and vent biota. We feel that, in addition to its historical value, the Challenger's metalliferous sediment collection provides: (1) the opportunity to investigate a set of sediments from an area of the Pacific where data (geochemical and mineralogical) are relatively scarce; and (2) the possibility to investigate the pre-industrial isotopic signature (including the rather novel, non-traditional Fe and Zn isotopes) in marine sediments. We have revisited these samples in order to provide a detailed mineralogical and geochemical description, and we report our data in this contribution.

2. GEOLOGIC SETTING

On her way back to Britain, the H.M.S. Challenger crossed the SE Pacific carrying out a transect (Sites ##292–297; Fig. 1) sampling of the seafloor with a complex tectonic history. This region, where the Pacific, Antarctic and Nazca plates interact, is characterized by northward migration of the Pacific–Antarctic–Nazca triple junction and its predecessor, the Pacific–Antarctic–Farallon triple junction during the last ~46 Ma (Bird et al., 1999). This evolution has included ridge propagation, microplate formation and microplate abandonment (Bird et al., 1999), which has left a legacy of fossil microplates (Hudson, Friday) embedded in the Antarctic plate (Tebbens and Cande, 1997). Rift propagation formed the Juan Fernandez
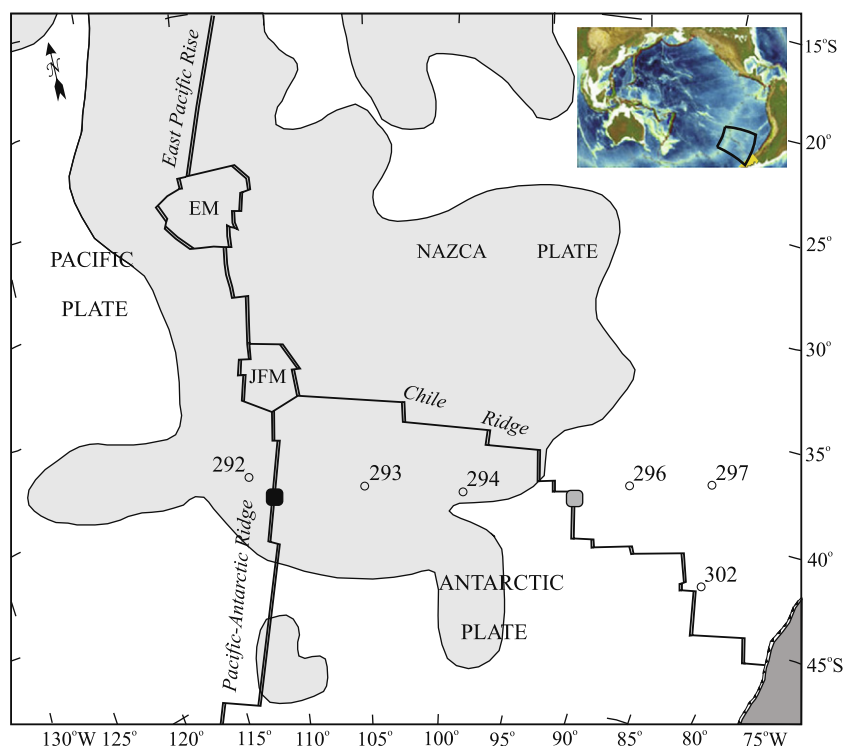

Fig. 1. Location map of the study region in the southeast Pacific Ocean (confined at the inset map of the Pacific). Shadowed in light grey = fields of metalliferous sediments (Gurvich, 2006); shadowed in dark grey = South America Plate; EM = Easter Microplate; JFM = Juan Fernandez Microplate; open circles = H.M.S. Challenger sampling sites (Murray and Renard, 1891); solid squares = known (black; FOUNDATION III cruise, R/V Sonne, Stoffers et al., 2002) and inferred (grey; GEOMETEP 4 cruise, R/V Sonne, Marienfeld and Marchig, 1992) hydrothermal fields; yellow painted southern end of South America (inset map) = Patagonia. (For interpretation of the references to colour in this figure legend, the reader is referred to the web version of this article.)

microplate (Fig. 1) at the present triple junction of East Pacific Rise (EPR), Pacific–Antarctic Ridge (PAR) and Chile Ridge (CR) (Bird et al., 1998). The seafloor spreading rates at the active plate boundaries in this region are currently the fastest on the planet (∼15 cm/yr; Hey et al., 2004). This unusual tectonic setting creates a high rate of tectonic and volcanic activity giving rise to unusual magmatic-hydrothermal systems (Baker et al., 2002; Hey et al., 2004). The extremely high hydrothermal activity in this region has resulted in the development of the largest field of metalliferous sediments in the Ocean (Gurvich, 2006). Its southern part has been delineated after several US (Boström, 1973) and Soviet Union (Gurvich, 2006) expeditions in the 1960s–1970s. Two hydrothermal fields that contribute to the southern extent of this metalliferous field have been found in the south-eastern part of the Pacific Ocean: one on the PAR (Stoffers et al., 2002) and another on the CR (Marienfeld and Marchig, 1992). The regional pattern of abyssal circulation (north-east resultant direction; Lonsdale, 1976) partly controls the dispersal of precipitates of the hydrothermal plume fallout and consequently the distribution of distal metalliferous sediments. It also influences the position of CCD that occurs at <4000 m in the studied area (Lonsdale, 1976).

3. MATERIAL AND METHODS

3.1. Samples

We selected and studied eight sediment samples taken by the H.M.S. *Challenger* at six sites (including the only site originally reported with metalliferous sediments, #293; Murray and Renard, 1891) situated along a transect crossing both the Pacific–Antarctic and the Chile Ridges (Tables 1 and 2 and Fig. 1). These sites are located at different seafloor morpho-structures: site 292 lies nearby the crest of PAR; site 293 is at PAR eastern flank; site 294 lies in the northern part of the SE Pacific Basin (northern part of

the Antarctic Plate); site 302 lies at the crest of CR; site 296 is at CR eastern flank; and site 297 is in the Chile Basin (southern part of the Nazca Plate) (Fig. 1). Five of the sites (##292, 293, 294, 296, 302) were supposed to be influenced by the hydrothermal activity at the two spreading ridges, while the sixth site (#297) was selected for study as a background site. Sampling details and original sample descriptions (Murray and Renard, 1891) are listed in Table 1. At four of the sites (##292, 293, 294, 302) only surface sediment was sampled, while at the other two sites (##296, 297) short sediment cores were recovered (Table 2). The incomplete description of these two cores (Murray and Renard, 1891) made it impossible to ascribe precisely the positions of the core samples and therefore we named the samples as "lower" and "upper", and "grey" and "light", respectively (Table 2) giving a tentative impression for their stratigraphic positions. After the post-cruise on-shore investigation of the sediments sampled during the cruise (Murray and Renard, 1891), the sediment collection was donated to the Natural History Museum (NHM), London. At the NHM this collection was kept in several rooms over the years and finally moved to the Wandsworth out-station where it is now housed at controlled temperature and humidity. The studied sediments were kept sealed in the original thick-wall glass jars and tubes (Fig. 2A and B). The samples were dry when the containers were opened, obviously the result of the long (over 100-year) storage. Thus, in our study we investigated these dry samples.

Previous studies at the PAR and CR crests (Marienfeld and Marchig, 1992; Stoffers et al., 2002) revealed that the axial zones of these ridges exposed fresh and weathered basalts. This implies the hydrothermal systems responsible for the formation of the metalliferous sediments in the studied region are basalt-hosted. Therefore, in order to investigate the Fe and Zn isotope fractionation during hydrothermal alteration of basement rocks and metalliferous sediment precipitation we analyzed two basalt samples recently collected from the axial zone of the CR (Fig. 1; Marienfeld

Table 1
Investigated samples of the voyage of H.M.S. *Challenger* (1872–1876).

Station #	NHM ID #	Date of collection	Sampling device	Latitude (S)	Longitude (W)	Depth (m)	Bottom seawater T (°C)	Description
292	M 363	29.10.1875	Sounding tube	38°43′0″	112°31′0″	2926.1	1.8	Globigerina ooze, light brown–grey, slightly coherent
293	M 364	01.11.1875	Sounding tube	39°04′0″	105°05′0″	3703.3	1.3	Globigerina ooze, brown, coherent, dark red–brown or chocolate coloured and plastic when wet
294	M 365	03.11.1875	Sounding tube	39°22′0″	98°46′0″	4151.4	1.4	Red clay, chocolate coloured when dry, coherent, homogeneous, rich chocolate colour and plastic when wet
296	M 367	09.11.1875	Sounding tube/ Trawl	38°06′0″	88°02′0″	3337.6	1.8	Globigerina ooze, light brown–grey when dry, somewhat coherent. Two layers were noticeable in the tube, a straw coloured upper and a dark brown lower
297	M 368	11.11.1875	Sounding tube	37°29′0″	83°07′0″	3246.1	1.9	Globigerina ooze, yellow–grey, slightly coherent. Yellow and grey coloured ooze in the tow-nets at the trawl
302	M 373	28.12.1875	Trawl	42°43′0″	82°11′0″	2651.8	2.0	Globigerina ooze, pale yellow–brown, slightly coherent, yellow–red and gritty when wet.

Table 2
Mineralogical composition (XRD) of H.M.S. *Challenger* (1872–1876) metalliferous sediments.

Station #	Sample #	Bulk mineralogy	Mineralogy of carbonate-free fraction
292	292	Calcite	Goethite (?), amorphous silicate (?), δ-MnO$_2$, kaolinite, mica, barite, plagioclase, quartz, K-feldspar
293	293	Calcite, goethite/amorphous silicate (?)	Goethite (?), amorphous silicate (?), δ-MnO$_2$, plagioclase, quartz, barite, kaolinite, mica, smectite (?), K-feldspar
294	294	Smectite (?), δ-MnO$_2$, mica, kaolinite, goethite/amorphous silicate (?)	Goethite (?), amorphous silicate (?), δ-MnO$_2$, anorthite, quartz, barite, phillipsite, kaolinite, mica, smectite (?), K-feldspar
296	296-upper	Calcite, plagioclase, quartz	Kaolinite, plagioclase, smectite, mica, quartz, chlorite, amphibole, goethite, barite
	296-lower	Calcite, plagioclase, quartz, goethite/amorphous silicate (?)	Not analyzed
297	297-light	Calcite, plagioclase, quartz, goethite/amorphous silicate (?)	Smectite, kaolinite, plagioclase, quartz, goethite, mica, chlorite, barite, amphibole
	297-grey	Plagioclase, quartz, calcite, smectite, kaolinite, chlorite (?), mica, amphibole (?)	Smectite, mica, kaolinite, chlorite, plagioclase, quartz, amphibole, talc (?), zeolite (?)
302	302	Calcite	Smectite, plagioclase, kaolinite, quartz, mica, chlorite, goethite, amphibole, barite

and Marchig, 1992) along with three metalliferous sediment samples (##292, 293, 294) for their Fe and Zn isotope composition. One of the basalt samples was fresh basalt (SO 40-31D) while the other was altered basalt (SO 40-38D). The altered basalt sample was subdivided into three subsamples: yellowish altered basalt (taken from within the rock specimen; SO 40-38D/1); red, hard surface of altered basalt (what was believed to correspond to heavily altered basalt from the rock surface; SO 40-38D/2); and red, soft precipitate on altered basalt (supposed to be metalliferous precipitate deposited on the basalt surface; SO 40-38D/3). These samples would provide an insight into the progressive alteration of basalt by the hydrothermal fluids and the precipitation of metalliferous sediment from the hydrothermal plume.

3.2. X-ray diffraction

Aliquots from all eight samples were finely ground in an agate mortar and their bulk mineralogy was studied using a position-sensitive detector X-ray diffractometer (Enraf–Nonius Powder Diffraction System 120 X-ray diffractometer with monochromatic Cu K$_\alpha$ radiation, 40 kV, 35 mA, 0.24 × 5 mm divergence slit and no receiving slit) on sedimented powder mounts, from 2 to 120° 2θ. This type of apparatus collects the diffracted radiation in the entire angular range simultaneously, using an arch-shaped detector. The angle between the incident beam and the sample plane was 2–3°. The samples were spun to maximize the analyzed volume and the counting time was 15 min. We used Si, Y$_2$O$_3$ and C$_{22}$H$_{44}$O$_2$·Ag for calibration. Since most of the samples were rich in biogenic calcite *Globigerina* oozes we studied the mineralogy of their carbonate-free fraction after calcite dissolution (2% acetic acid in water with stirring, ultrasonic treatment and centrifugation; the process was repeated three times and finally the solid was washed four times with distilled water by centrifugation). The calcite-free fraction was analyzed as oriented mounts to emphasize clay mineral peaks, as air-dry and glycolated

(overnight in ethylene glycol atmosphere at 60 °C) specimens. They were analyzed in a Philips PW 1050 diffractometer with Cu K$_\alpha$ radiation, at 42 kV and 42 mA, in the range 2–40° 2θ, at 0.02° 2θ steps and 10 s/step. Black magnetic micronodules (diameter $\sim$1 mm) were selected by hand-picking with a steel needle under stereo-microscope from washed (distilled water) and sieved (sieve mesh 100 μm) sample #294 and analyzed as random powder mounts in a Philips PW 1710 diffractometer with automatic divergence slit and monochromatic Cu K$_\alpha$ radiation, at 40 kV and 35 mA, in the range 5–80° 2θ, at 0.01° 2θ step and 2 s/step.

3.3. Microscopic studies

Scanning electron microscope (SEM) observations were made on C-coated specimens of: (1) fragments of bulk samples both as loose sediment and chips of hard dried sediment; (2) black micronodules. They were imaged with secondary and back-scattered electrons and chemically analyzed by means of EDX, using a JEOL 5900LV and a Leo 1455VP electron microscopes both equipped with an Oxford Instruments INCA EDX detector. Chemical analyses were calibrated using standard reference minerals.

3.4. Magnetic mineralogy

Various magnetic parameters have been determined to gain further understanding of the mineralogy of Fe-containing phases of the samples, following Dekov et al. (2009). Magnetic measurements are in particular very sensitive to minor amounts of magnetically ordered minerals such as Fe-oxyhydroxides. Five powdered samples were compacted into plastic cubes (2 cm edge) and used to measure: (1) the low field magnetic susceptibility (χ) using a MFK1 instrument (Agico), and (2) the anhysteretic remanent magnetization [ARM, in a 120 mT alternating field (AF) and 0.1 mT bias field] and the saturation isothermal remanent magnetization (IRM, in 3 T) using a 2G DC
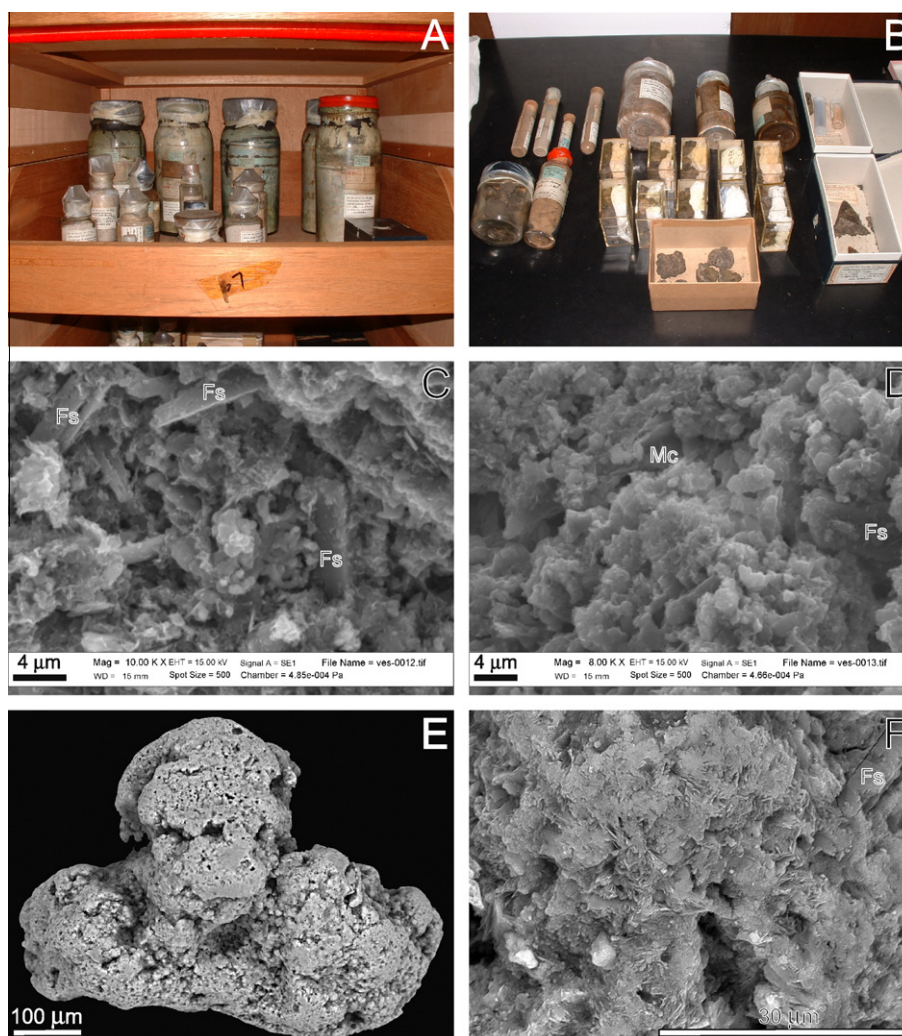
Fig. 2. (A and B) Photographs of the H.M.S. *Challenger* metalliferous sediment collection stored in the Wandsworth out-station (Natural History Museum, London). (C and D) SEM microphotographs (SEI) of bulk metalliferous sediment (H.M.S. *Challenger* Site #294) composed of poorly-crystalline and X-ray amorphous Fe–Mn-oxyhydroxides and Si–Al–Mg gels (?). Note, the relatively intact feldspar (Fs) grains and mica (Mc) flakes scattered in the Fe–Mn-oxyhydroxide + Si–Al–Mg gel (?) matrix suggesting that this matrix is not a result of dissolution of detrital minerals. (E and F) SEM microphotographs (SEI) of Fe–Mn micronodule (sample #294) composed of goethite and MnO_2 (vernadite?) crystals (close up at (F)).

SQUID cryogenic magnetometer. IRM was submitted to alternating field demagnetization up to 120 mT. Hysteresis measurements were conducted on a coherent (solid) fragment of sample #294 using a Micromag vibrating sample magnetometer (VSM). χ, ARM and IRM were mass normalized, but we found it useful to further normalize them to Fe content (in wt.%) of the samples in order to discuss the partitioning of Fe into its various mineral phases. The relative error on χ, ARM and IRM measurements was better than 1% because all the samples were quite strongly magnetic. After resuspension of an aliquot of sample #294 in distilled water the subsample was wet-sieved (sieve mesh 100 μm). The magnetic sub-fraction was extracted from the >100 μm grain-size fraction and investigated for micrometeorites (cosmic spherules) under optical microscope.

3.5. Major, trace and rare earth element analyses

Major elements in bulk, powdered sediment samples were measured using ICP-AES (Varian VISTA PRO) and trace and rare earth elements (REE) were analyzed using ICP-MS (Varian 800). Total dissolution of the bulk sample was performed by HF–$HClO_4$–aqua regia attack in closed bottles in a microwave oven (Thompson and Walsh, 2003). The accuracy of the analytical results was controlled by measuring the international standard reference materials SCo-1, JSd-1, MAG-1 and JLK-1. Analytical errors for ICP-AES were 0.4–5% of the measured values. Errors for ICP-MS were 0.02–22% of the measured value depending on the concentration, with typical values <15%.

Total C and total organic C was measured by carbon–hydrogen–nitrogen (CHN) elemental analysis using a CE

Elantech Flash 1112 EA Soil Analyzer. Samples were heated at 500 °C (organic C) and 900 °C (total C) and the resulting CO_2, H_2O and NO_3 gases quantified and converted into atomic weight percentages. Blanks and aspartic acid standard were also analyzed. The analytical error is <5% of measurement. The detection limit is 0.07% C. Content of $CaCO_3$ was calculated on the basis of $C_{tot.}$ and $C_{org.}$ concentrations and used to recalculate element concentrations on a carbonate-free basis.

3.6. Isotope analyses

Bulk sediment samples were subjected to sequential leaching and leachates and residues were analyzed for Sr, Nd, and Pb isotopes. About 100 mg of pulverized bulk sediment was treated with 1 M (Optima) acetic acid. Two instalments of 5 ml aliquot were added to the bulk sediment allowing enough time for the acetate-soluble fraction of the sediment to react with the acid and degas. After the degassing ceased, the solution was centrifuged and 2 ml of the supernatant were dried down in clean Teflon vials for column chemistry. The resultant bulk sediment was thoroughly cleaned with 4× distilled water until all traces of the acetic acid had been removed and residue was dried before moving to the next extraction step. The dried samples were treated with 4 ml 2 M HCl in order to remove any residual phases that can carry seawater and/or a hydrothermal signal, following Nielsen et al. (2007). Samples were again centrifuged and 2 ml of the supernatant were separated and dried down for column chemistry. The final step involved complete digestion of the residual aluminosilicate fraction in HF–HNO₃ mixture.

Foraminifera (*Globigerina bulloides*) concentrates were collected by hand-picking with a steel needle under the stereo-microscope from four samples (##292, 293, 296, 297), dissolved in 1 M acetic acid (Optima), and analyzed for Pb isotopes as described above.

Sr, Nd, and Pb isotopes were determined on a "Nu-Plasma" MC-ICP-MS, following methods described in Kamenov et al. (2008). The reported $^{87}Sr/^{86}Sr$ ratios are relative to NBS 987 $^{87}Sr/^{86}Sr = 0.710246$ (+/−0.000030, 2σ) and the reported Nd isotopic compositions are relative to JNdi-1 $^{143}Nd/^{144}Nd = 0.512103$ (+/−0.000018, 2σ). Pb isotopic compositions were determined with Tl normalization and the Pb isotope data are relative to the following values of NBS 981: $^{206}Pb/^{204}Pb = 16.937$ (+/−0.004, 2σ), $^{207}Pb/^{204}Pb = 15.490$ (+/−0.003, 2σ), and $^{208}Pb/^{204}Pb = 36.695$ (+/−0.009, 2σ).

100 mg of each of the four basalt and three metalliferous sediment (##292, 293, 294) samples were dissolved in 5 ml 20 M HF and 2 ml 15 M HNO₃ at 120 °C on a hotplate for 48 h. Solutions were evaporated to dryness and the residues were re-dissolved in 2.5 ml 7 M HCl containing 0.001% H_2O_2. Each solution was split into three aliquots: 0.5 ml for concentration measurements (Al, Fe, Zn, Mn, Cu, Ni, and Co), 1 ml for Fe and Zn isotope analysis and 1 ml for archive. The 0.5-ml aliquot (of the basalt samples only) was made up to 3.5 ml 1 M HCl prior to concentration measurements on a Varian VISTA PRO ICP-AES, for which analytical errors were between 0.4 and 5% of the measured values.

A spike mixed predominantly from ^{64}Zn and ^{67}Zn was added to the 1-ml aliquots such that the sample-spike mixture had a $^{64}Zn:^{66}Zn:^{67}Zn:^{68}Zn$ ratio of 5.3:1.4:1.5:1 (this was necessary for the Zn double spike mass bias correction procedure – see below). Zinc and Fe were then separated from the matrix using ion exchange chromatography as detailed elsewhere (Chapman et al., 2006). Zinc and Fe fractions were re-dissolved in 0.1 M and 0.5 M HNO₃, respectively, in preparation for the MC-ICP-MS. The isotope measurements were conducted on a HR "Nu-Plasma" MC-ICP-MS (Nu Instruments). For the Zn isotopes a double spike technique was used to correct for mass bias. The data acquisition sequence of the main run comprised 60 integrations of 5 s each, in blocks of 20. Prior to each block, the baseline signals were monitored for 15 s, whilst the ion beam was deflected in the electrostatic analyzer. These data were subsequently subtracted from the measured ion beam intensities. Given a predetermined isotope composition of the spike and standard reference material (London Zn), the natural isotope composition of the sample could be determined by inversion using a spreadsheet-based implementation of the iterative methods (Siebert et al., 2001).

For Fe the HR "Nu-Plasma" apparatus was set up in pseudo high resolution in order to resolve $^{40}Ar^{14}N^+$, $^{40}Ar^{16}O^+$ and $^{40}Ar^{16}OH^+$ that form isobaric interferences with ^{54}Fe, ^{56}Fe and ^{57}Fe, respectively (Arnold et al., 2008). Also the dynamic range of the amplifiers was extended from 10 to 20 V (on 10^{11} Ω resistors), thus improving the signal to amplifier noise ratio and the precision of the higher dynamic range isotopic ratio $^{57}Fe/^{54}Fe$. The standard sample bracketing technique was implemented for mass bias correction (Mullane et al., 2003). The data acquisition sequence was as described above for Zn, however, the main run comprised only 25 integrations.

Potential interferences during the Fe isotope measurements were tested using three isotope plots and the slopes always lied within the one predicted from the kinetic and equilibrium laws (Young et al., 2002).

Isotope ratios are reported in δ-notation where $\delta^{66}Zn = [(^{66}Zn/^{64}Zn)_{sample})/(^{66}Zn/^{64}Zn)_{standard} - 1] \times 10^3$, and where $(^{66}Zn/^{64}Zn)_{sample}$ is the isotope ratio of the sample and $(^{66}Zn/^{64}Zn)_{standard}$ is the isotope ratio the standard reference material. Similarly, $\delta^{56}Fe = [(^{56}Fe/^{54}Fe)_{sample})/(^{56}Fe/^{54}Fe)_{standard} - 1] \times 10^3$. All δ-values are reported relative to JMC 3-0749L for Zn and IRMM-14 for Fe.

Accuracy of the isotope measurements was tested by analysis of the single element solutions and natural standard reference materials and ensuring values corresponded with long term averages. The standard reference materials and corresponding long term values are $\delta^{66}Zn = -7.07 \pm 0.08‰$ (Spec-pure Zn), $\delta^{66}Zn = +0.08 \pm 0.04‰$ (London Zn), $\delta^{66}Zn = 0.25 \pm 0.06‰$ (BCR 027 Blend Ore), $\delta^{56}Fe = 0.44 \pm 0.04‰$ (Johnson Matthey Fe) and $\delta^{56}Fe = 0.10 \pm 0.04‰$ (Puratronic Alfa Aesar Fe). Errors on the reported δ-values are $\pm 2\sigma$ calculated from a minimum of three replicate analyses. Procedural blank contributions were typically 20 ng of Zn and 40 ng of Fe, making contribution to the sample isotopic composition insignificant.

4. RESULTS

4.1. Mineralogy

Most of the investigated samples were originally described as *Globigerina* oozes with varying colour and only one (#294) was characterized as red clay (Table 1). Our XRD study (Table 2) revealed some broad peaks with low intensity, one corresponding to a poorly-crystalline Mn-oxide (δ-MnO_2) and some which could not be assigned with certainty and we ascribed them to poorly crystallized goethite and smectite and to an amorphous silicate phase (with question marks in Table 2 and in the text). The XRD analyses of bulk (untreated) samples showed that the major mineral in 6 of them was calcite with subordinate amounts of goethite (?), amorphous silicate (?), plagioclase and quartz (Table 2). One sample (#294) contains mainly smectite (?), goethite (?), amorphous silicate (?) and δ-MnO_2, and another (#297-grey) is composed largely of plagioclase, quartz, calcite and smectite (Table 2). The magnetic extract of sample #294 shows, in addition to the above-mentioned minerals, phillipsite [$(Na,K,Ca)_{1-2}(Si,Al)_8O_{16}$ $6H_2O$]. According to the mineralogy of the carbonate-free fraction, the studied samples can be divided in two groups: (1) sediments with major minerals goethite (?), δ-MnO_2 and amorphous silicate (?), and minor minerals plagioclase, quartz, barite, kaolinite and mica (##292, 293, 294); and (2) sediments with major minerals smectite, plagioclase, kaolinite, quartz, mica, and minor goethite (##296-upper, 296-lower, 297-light, 297-grey, 302) (Table 2).

SEM-EDX studies of the sediments from the first group revealed they were composed, apart from the biogenic calcite, of a fine-grained matrix of Fe–Mn-oxyhydroxides and Si–Al–Mg gels with scattered grains of quartz, plagioclase and mica (Fig. 2C and D). This oxyhydroxide-silicate matrix has the appearance of colloidal aggregates with very fine septal crystals on their surface (Fig. 2C and D), which implies incipient stage of colloidal crystallization. Black micronodules (Fig. 2E) composed of aggregates of goethite and δ-MnO_2 crystals (Fig. 2F) were found in appreciable amounts only in sample #294. The scattered quartz, plagioclase and mica grains were intact and did not show signs of dissolution. The minerals which composed the sediments from the second group often exhibited broken apexes and edges which implies they were detrital and probably a result of aeolian transport.

Magnetic parameters of the samples after normalized to Fe content are quite constant (excepting sample #302) despite an order of magnitude variation of Fe concentration (Table 3). Theoretical paramagnetic susceptibility was calculated (χ_p in Table 3) assuming all Fe as Fe^{3+} and Mn as Mn^{4+} (Rochette and Lamarche, 1986). The microscopic investigation of the magnetic sub-fraction of sample #294 revealed numerous black, earthy and fragile micronodules and crusts, but no identifiable cosmic spherules.

4.2. Geochemistry

One of the studied samples (#297-grey) differs substantially from the others: it has very low $CaCO_3$ (in agreement with its mineral content), Sr, Ba, Mo, Ni and Pb contents, very high Si, Al, Ti, Rb, Cs, Ga and Cr concentrations, and high Al/(Al + Fe + Mn) and Fe/Mn ratios (Table 4). The samples from near the ridge crests (##292, 293, 296, 302) at water depths above the CCD ($\sim$4000 m) have high $CaCO_3$ content (Table 4). Only one (#294) is from beneath the CCD and consequently has very low $CaCO_3$ content. Samples ##292, 293, 294 and 296-lower have similar geochemical features (although different $CaCO_3$ content): $Fe_{CFB} > 10$ (CFB = carbonate-free basis), $Mn_{CFB} > 3$, Al/(Al + Fe + Mn) < 0.3, high content (on a carbonate-free basis; not given in Table 4) of As, Ba, Be, Bi, Cd, Co, Cu, Mo, Ni, Pb, Sb, Th, Tl, U, V, W, Y, Zn, Zr (Table 4). The other three samples (##296-upper, 297-light, 302) have $Fe_{CFB} < 10$, $Mn_{CFB} < 3$, 0.3 < Al/(Al + Fe + Mn) < 0.4, and relatively low concentrations of the above mentioned microelements.

The chondrite-normalized REE distribution pattern of sample #297-grey exhibits a slightly positive Ce anomaly ($Ce/Ce^* > 1$), slightly negative Eu anomaly ($Eu/Eu^* < 1$), and an enrichment of light REE (LREE) relative to heavy REE (HREE) ($La_N/Lu_N > 1$) (Fig. 3 and Table 4). REE distribution patterns (on a carbonate-free basis) of the rest of the studied samples show similar features: slightly negative Ce anomaly, slightly negative to slightly positive Eu anomaly, and enrichment of LREE relative to HREE (Fig. 3 and Table 4). The REE distribution patterns of four of these samples (##292, 293, 294, 296-lower) differ a little from those of the other three samples with their more pronounced negative Ce anomaly (Fig. 3 and Table 4) and somewhat higher ΣREE (Table 4). All the REE patterns have nearly flat HREE distributions.

4.3. Isotope data

Pb isotopes (Table 5) show a $^{206}Pb/^{204}Pb$ range from 18.38 to 18.7, with leachates showing less-radiogenic values

Table 3
Magnetic parameters of H.M.S. *Challenger* (1872–1876) metalliferous sediments.

Station #	Sample #	χ (10^{-8} m^3/kg)	χ_p (10^{-8} m^3/kg)	ARM (mA m^2/kg)	IRM (mA m^2/kg)	IRM_{res} (%)	χ/Fe (10^{-8} m^3/kg)	ARM/Fe (mA m^2/kg)	IRM/Fe (mA m^2/kg)
292	292	12.2	9.4	0.186	1.43	3.0	508	7.7	59.6
293	293	98.6	49.6	1.49	11.8	4.8	759	11.5	91.0
294	294	136.8	76.6	2.89	18.0	4.2	667	14.1	88.0
296	296-lower	34.2	22.8	0.404	5.79	7.8	562	6.6	95.3
302	302	10.8	2.7	0.051	1.12	7.7	1415	6.7	147.3

Table 4

Chemical composition of H.M.S. *Challenger* (1872–1876) metalliferous sediments.

Station #	Sample #	Si (wt.%)	Ti	Al	Fe	Fe$_{CFB}$	Mn	Mn$_{CFB}$	Mg	Ca	Na	K	P	C$_{tot}$	C$_{org}$	CaCO$_3$[a]	Al/(Al+Fe+Mn)	Fe/Mn	As (ppm)	Ba	Be	Bi	Cd	Co	Cr	Cs	Cu	Ga	Ge	Hf	Li	Mo	Nb
292	292	0.67	0.01	0.14	2.40	13.2	0.94	5.20	0.23	37.9	0.15	0.03	0.07	11.1	1.28	81.9	0.04	2.55	43.4	1422	0.23	10.8	1.22	12.2	7.27	0.06	126	0.43	0.08	0.22	1.88	10.3	0.64
293	293	3.98	0.14	1.38	13.0	26.7	4.10	8.42	0.71	21.7	0.25	0.27	0.33	6.15	b.d.l.[b]	51.2	0.07	3.18	141	3583	1.59	60.8	0.78	62.2	10.3	0.47	839	4.80	0.62	2.61	7.60	95.1	6.87
294	294	13.5	0.28	4.16	20.5	20.5	5.39	5.40	1.69	1.60	0.93	1.28	0.52	0.24	0.23	0.01	0.14	3.80	225	10650	2.82	146	0.95	140	12.3	1.46	1498	14.4	1.37	6.59	28.7	157	15.8
296	296-upper	2.08	0.05	0.73	1.27	8.36	0.36	2.35	0.23	37.3	0.26	0.14	0.06	10.6	0.38	84.8	0.31	3.56	12.0	1197	0.22	12.2	0.32	12.0	10.0	0.42	92.5	1.69	0.14	0.42	5.09	4.44	1.10
	296-lower	9.53	0.20	3.19	6.08	11.1	1.66	3.03	0.94	21.2	0.66	0.80	0.16	6.01	0.59	45.2	0.29	3.67	65.8	6447	1.09	55.2	3.46	62.7	20.9	2.03	501	8.59	0.80	2.44	23.9	49.4	5.47
297	297-light	3.17	0.08	1.18	1.74	6.49	0.40	1.50	0.31	35.5	0.29	0.20	0.06	9.33	0.54	73.2	0.36	4.34	13.4	2703	0.34	15.3	0.51	18.9	13.4	0.68	125	2.74	0.23	0.67	8.32	3.65	1.61
	297-grey	25.5	0.57	9.09	5.47	5.48	0.07	0.07	1.55	2.48	2.20	1.61	0.10	1.23	1.21	0.18	0.62	75.3	14.8	305	1.54	17.2	0.53	17.2	45.9	5.25	100	21.0	1.46	2.71	49.5	2.56	6.07
302	302	1.84	0.03	0.53	0.76	4.98	0.09	0.59	0.20	35.5	0.28	0.11	0.02	10.5	0.28	84.8	0.38	8.44	13.2	1104	0.15	6.51	0.29	5.24	12.8	0.31	53.1	1.26	0.10	0.21	4.55	0.70	0.63

Station #	Sample #	Ni (ppm)	La	Ce	Pr	Nd	Sm	Eu	Gd	Tb	Dy	Ho	Er	Tm	Yb	Lu	ΣREE	(Ce/Ce*)[c]	(Eu/Eu*)[d]	La$_N$/Lu$_N$	Pb	Rb	Sb	Sc	Sn	Sr	Ta	Th	Tl	U	V	W	Y	Zn	Zr
292	292	88.6	16.5	11.8	3.30	14.1	2.96	0.95	3.42	0.57	3.69	0.80	2.42	0.35	2.27	0.34	63.5	0.37	0.91	5.14	197	1.09	1.03	1.42	22.7	1335	0.01	0.54	0.84	0.57	72	1.15	28.4	68.3	26.4
293	293	635	102	71.0	22.6	91.7	18.8	5.19	19.7	3.47	21.2	4.40	12.7	1.72	10.9	1.66	387	0.35	0.82	6.58	76.8	8.06	7.04	7.70	1.51	1038	0.22	2.61	3.18	2.09	330	7.02	136	226	191
294	294	1116	147	137	39.3	148	36.3	10.2	31.4	6.44	38.2	7.66	22.0	2.98	18.8	2.86	648	0.43	0.90	5.50	131	30.2	14.8	16.4	6.21	529	0.64	6.48	3.07	3.01	505	10.2	246	404	362
296	296-upper	81.6	14.7	14.8	3.41	13.9	3.06	0.94	3.62	0.58	3.66	0.78	2.36	0.33	2.10	0.32	64.6	0.49	0.86	4.95	16.9	5.85	0.63	3.20	2.72	1212	0.04	0.99	0.38	0.31	30.9	0.93	28.4	33.9	26.2
	296-lower	539	45.2	63.9	10.4	43.8	9.60	3.33	10.6	1.76	10.8	2.23	6.60	0.90	5.79	0.90	216	0.70	1.01	5.40	579	28.9	5.53	12.0	79.8	894	0.20	4.15	2.44	1.18	164	4.69	75.8	384	139
297	297-light	95.5	13.1	18.9	3.09	13.1	2.86	1.06	3.14	0.52	3.23	0.67	2.00	0.28	1.80	0.28	63.9	0.70	1.08	5.09	35.0	8.73	0.77	4.41	8.33	1368	0.06	1.28	0.73	0.39	44	0.96	24.0	44.9	37.2
	297-grey	b.d.l.	12.4	29.3	3.67	16.8	3.75	0.98	3.02	0.55	3.18	0.62	1.84	0.26	1.71	0.25	78.3	1.05	0.86	5.34	27.2	62.8	1.54	17.1	4.06	298	0.41	4.91	0.34	1.50	172	0.96	25.4	123	169
302	302	b.d.l.	4.80	6.51	1.00	4.29	0.92	0.38	1.10	0.18	1.20	0.27	0.85	0.12	0.82	0.12	22.6	0.69	1.14	4.15	1992	4.90	1.18	2.41	2.58	1173	0.03	0.52	0.06	0.16	15.7	0.32	11.1	28.6	b.d.l.

[a] Calculated using C$_{tot}$ and C$_{org}$.

[b] b.d.l. = below detection limit.

[c] Ce/Ce* = 2Ce$_N$/(La$_N$ + Pr$_N$).

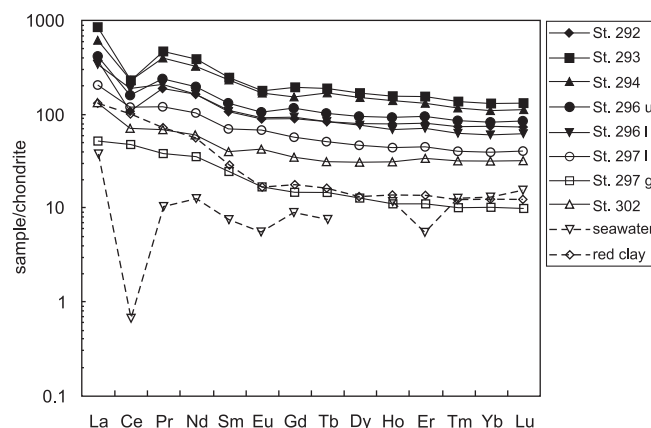[d] Eu/Eu* = 2Eu$_N$/(Sm$_N$ + Gd$_N$).

Fig. 3. C1 chondrite-normalized (Sun and McDonough, 1989) REE distribution patterns of the studied sediments (on a carbonate-free basis) from the H.M.S. *Challenger* voyage. Seawater = deep (3250 m) Pacific seawater (de Baar et al., 1985) $\times 10^6$; red clay = upper red clay, ODP Site 1215, Central Pacific (Ziegler et al., 2007).

than residues. Sr isotopes for leachates are overall similar to modern seawater with exception of sample #297-grey, which shows less-radiogenic values, with $^{87}Sr/^{86}Sr = 0.70835$ (Table 5). Residues, on the other hand, show much wider variations in their Sr isotopic signature, ranging from 0.70458 to 0.70997 for $^{87}Sr/^{86}Sr$. Leachates have relatively uniform ε_{Nd} around -5 (± 1) with exception of sample #297-grey ($\varepsilon_{Nd} = +2.5$). Compared to the leachates, the residues show slightly higher values with ε_{Nd} ranging from -4.8 to $+2.8$. Selected foraminifera shells (*G. bulloides*)

Table 5
Pb, Sr, and Nd isotope data for H.M.S. *Challenger* (1872–1876) metalliferous sediments leachates and residues.

	$^{206}Pb/^{204}Pb$	$^{207}Pb/^{204}Pb$	$^{208}Pb/^{204}Pb$	$^{87}Sr/^{86}Sr$	Error	$^{143}Nd/^{144}Nd$	Error	εNd
1 M CH₃COOH leachates								
St. 292	18.411	15.641	38.439	0.709180	0.000017	0.512370	0.0000078	−5.2
St. 293	18.632	15.593	38.399	0.709272	0.000015	0.512327	0.0000072	−6.1
St. 294	18.589	15.606	38.441	0.709156	0.000014	0.512340	0.0000043	−5.8
St. 296-upper	18.492	15.618	38.444	0.709110	0.000013	0.512370	0.0000047	−5.2
St. 296-lower	18.401	15.633	38.472	0.709089	0.000015	0.512404	0.0000077	−4.6
St. 297-light	18.449	15.636	38.463	0.709179	0.000022	0.512388	0.0000100	−4.9
St. 297-grey	18.518	15.622	38.497	0.708348	0.000007	0.512767	0.0000087	2.5
St. 302	18.390	15.640	38.424	0.709148	0.000016	0.512420	0.0000071	−4.3
2 M HCl leachates								
St. 292	18.427	15.635	38.427	–	–	–	–	–
St. 293	18.684	15.596	38.420	–	–	–	–	–
St. 294	18.638	15.609	38.463	–	–	–	–	–
St. 296-upper	18.512	15.612	38.429	–	–	–	–	–
St. 296-lower	18.417	15.641	38.494	–	–	–	–	–
St. 297-light	18.480	15.633	38.470	–	–	–	–	–
St. 297-grey	18.528	15.619	38.501	–	–	–	–	–
St. 302	18.393	15.644	38.435	–	–	–	–	–
Residues								
St. 292	18.434	15.633	38.432	0.709973	0.000034	0.512390	0.000008	−4.8
St. 293	18.698	15.595	38.432	0.707680	0.000010	0.512396	0.000008	−4.7
St. 294	18.685	15.602	38.468	0.708635	0.000008	0.512409	0.000005	−4.5
St. 296-upper	18.546	15.616	38.490	0.706606	0.000012	0.512549	0.000021	−1.7
St. 296-lower	18.413	15.628	38.468	0.707937	0.000009	0.512551	0.000006	−1.7
St. 297-light	18.552	15.623	38.515	0.706065	0.000011	0.512621	0.000006	−0.3
St. 297-grey	18.593	15.607	38.500	0.704587	0.000012	0.512782	0.000006	2.8
St. 302	18.396	15.642	38.436	0.708086	0.000013	0.512521	0.000007	−2.3
Foraminifera								
St. 292	18.484	15.624	38.437	–	–	–	–	–
St. 293	18.612	15.623	38.467	–	–	–	–	–
St. 296	18.381	15.618	38.372	–	–	–	–	–
St. 297	18.421	15.627	38.423	–	–	–	–	–

Table 6
Fe and Zn isotope data for the H.M.S. *Challenger* (1872–1876) metalliferous sediments and reference basalt samples.

Sample #	Description	Al[a] (wt.%)	Fe (wt.%)	EF_{Fe}[b]	$\delta^{56}Fe$ (‰)	$\pm 2\sigma$	Zn (ppm)	EF_{Zn}	$\delta^{66}Zn$ (‰)	$\pm 2\sigma$
292	Metalliferous sediment	0.76	13.2	–	−0.39	0.04	378	–	+0.40	0.06
293	Metalliferous sediment	2.83	26.7	–	−0.34	0.07	464	–	+0.44	0.10
294	Metalliferous sediment	4.16	20.5	–	−0.32	0.07	404	–	+0.37	0.09
SO 40–38D/3	Red, soft precipitate on altered basalt	3.14	18.8	6.5	−0.22	0.05	457	16.2	+0.72	0.08
SO 40–38D/2	Red, hard surface of altered basalt	1.94	17.0	9.5	−0.22	0.10	414	23.7	+0.67	0.08
SO 40–38D/1	Yellowish altered basalt	7.94	9.10	1.3	+0.10	0.11	505	7.1	−0.10	0.15
SO 40–31D	Fresh basalt	7.53	6.93	1	+0.14	0.04	70	1	+0.29	0.07

[a] Al, Fe and Zn concentrations recalculated on carbonate-free basis for the sediments only.

[b] $EF_{element} = (element/Al)_{sample}/(element/Al)_{fresh\ basalt}$.

have a Pb isotope composition similar to that of the sediments.

The Fe–Zn-isotope composition of the fresh, unaltered basalt (SO 40-31D, $\delta^{56}Fe = 0.14 \pm 0.04$‰, $\delta^{66}Zn = 0.29 \pm 0.07$‰) agrees with previously published values for fresh, unaltered igneous rocks ($\delta^{56}Fe \sim 0.1$‰, Anbar and Rouxel, 2007; $\delta^{56}Fe = 0.11–0.12$‰, Teng et al., 2008; $\delta^{66}Zn = 0.17–0.41$‰, Chapman et al., 2006; $\delta^{66}Zn = 0.2–0.5$‰, Cloquet et al., 2007). In comparison, the altered basalt and metalliferous sediments are, in general, isotopically lighter for Fe and isotopically heavier for Zn (Table 6, $\Delta^{66}Zn_{unaltered-altered} < 0$ and $\Delta^{56}Fe_{unaltered-altered} > 0$). The slightly altered basalt (SO 40-38/1) shows $\delta^{56}Fe$ almost identical to the fresh basalt while Zn is isotopically lighter than all the other samples. It is important for our interpretations (Section 5.5) to know the nature of the several subsamples of the altered basalt sample and therefore we present also (Table 6) the concentrations of Al, Fe and Zn, and enrichment factors (EF) for the investigated hard rock samples (initially assuming all subsamples of SO 40-38D represent basalt altered at different extent). A plot of Zn concentration versus Fe and Al content of the *Challenger* samples, after calcite subtraction (not shown), showed the expected negative correlation between Fe, represented mainly in FeOOH, and Al, present in the aluminosilicate phases. Zinc showed a broad positive correlation with Fe, indicating that Zn is mainly located in the FeOOH phases and its isotope signature is dominated by Zn in FeOOH.

5. DISCUSSION

5.1. Identification of metalliferous sediments: geochemical constraints

The question of the nature of metalliferous sediments is generally considered solved and, reasonably, it receives little recent scientific attention. However, the careful reading of the literature indicates that there is no common, widely accepted quantitative criterion for the differentiation of metalliferous sediments from the other similar Fe–Mn-rich deposits, which causes confusion. The essential feature of a metalliferous sediment is that it is a hydrothermal Fe–Mn deposit that forms near active plate boundaries and hot spots (Bonatti, 1981). With surprising insight for that early stage of oceanographic investigation, the scientists studying the *Challenger* samples realized that Fe and Mn could be supplied to the sediment from three main sources: (1) seawater; (2) submarine volcanism; (3) diagenetic processes (Murray and Renard, 1891; Murray and Irvine, 1895). Further development of this idea (Bonatti et al., 1972) led to the use of the element source as the main criterion in the genetic classification of the seafloor Fe–Mn deposits.

There are a number of quantitative criteria for differentiation of metalliferous (hydrothermal) sediments from the other types of seafloor Fe–Mn deposits, all of them based on geochemical features. Some classifications (Lisitzin et al., 1976; Strahov, 1976) use simple, easily applicable criteria. However, they often cannot distinguish between metalliferous (hydrothermal) and hydrogenous (hydrogenetic + diagenetic) deposits. For instance, Strahov (1976) considers as metalliferous (hydrothermal) those sediments in which $[(Fe + Mn)/Ti] > 25$. For Lisitzin et al. (1976) metalliferous are those sediments with Fe > 10 wt.% (on a carbonate- or biogenic silica-free basis). The application of these criteria leads to the inclusion of a number of hydrogenetic and diagenetic Fe–Mn deposits in the hydrothermal (metalliferous) group. Moreover, the latter criterion excludes all Mn-rich hydrothermal (metalliferous) sediments that do not contain Fe > 10 wt.% on an abiogenic basis. Other differentiation criteria (Boström, 1973; Marchig, 1978) are clear and precise, but arduous to use as they are based on several elemental ratios. For example, Boström (1973) considers metalliferous those sediments with all three conditions $[Fe/(Al + Fe + Mn)] > 0.5$, $[Al/(Al + Fe + Mn)] < 0.3$ and $[(Fe + Mn)/Al] > 2.5$.

Metalliferous sediments are enriched in Fe and Mn and depleted in Al (and Ti) relative to pelagic background sediments. At the same time, however, they are depleted in transition metals relative to the hydrogenetic Fe–Mn deposits. Thus, the ternary diagram by Bonatti et al. (1972) (Fig. 4) is very effective in differentiating Fe–Mn deposits and widely used. This approach, however, fails to differentiate diagenetic Fe–Mn deposits from hydrothermal deposits rich in Mn.
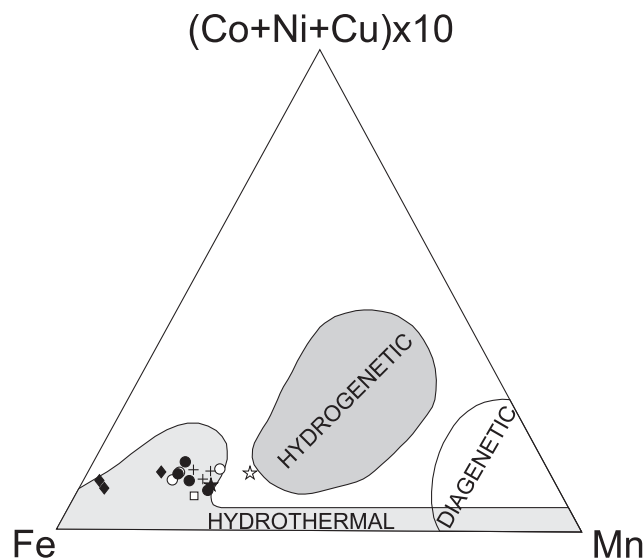
Fig. 4. Mn–Fe–(Co + Ni + Cu) × 10 ternary diagram of seafloor Fe–Mn deposits (after Bonatti et al., 1972): closed circles = H.M.S. *Challenger* metalliferous sediments, open circles = Bauer Deep metalliferous sediments (Sayles et al., 1975), crosses = PAR metalliferous sediments (Migdisov et al., 1979), open square = 42°S PAR metalliferous sediments (average; Walter and Stoffers, 1985), closed diamonds = Pacific pelagic red clays (Bischoff et al., 1979; Migdisov et al., 1979), open star = red, hard surface of altered basalt (sample SO 40-38D/2), closed star = red, soft precipitate on altered basalt (sample SO 40-38D/3).

We have plotted the data for four of the studied samples (##292, 293, 294, 296-lower), the richest in Fe (Fe$_{CFB}$ > 10 wt.%) and Mn (Mn$_{CFB}$ > 3 wt.%), on this ternary diagram (Table 7 and Fig. 4, black circles). For comparison, we have also plotted the data for the following sediments. (1) Surface metalliferous sediments taken in 1976 along a transect (parallel to 39°S) very close to the *Challenger* transect (parallel to ~39°S): St. 1002, close to *Challenger* St. 292; St. 999, close to *Challenger* St. 293; and St. 997, close to *Challenger* St. 294; (2) average surface metalliferous sediment taken at the PAR crest at 42°S; (3) surface metalliferous sediments at Bauer Deep; (4) Pacific surface pelagic red clays (Table 7 and Fig. 4). These metalliferous sediments plot close to each other in the hydrothermal field of the ternary diagram. Surprisingly, the Pacific pelagic red clays also fall into this field (Fig. 4), which suggests that the combined concentrations of Fe, Mn and transition elements cannot be used as a single, unambiguous criterion for differentiation of metalliferous sediments from the other types of sediments. What differentiates metalliferous sediment from pelagic red clay with similar appearance and some similar geochemical characteristics (transition metal content) is their Al (and Ti) content: metalliferous sediment is depleted in Al (and Ti) (Table 7). This feature, which was recognized years ago (Boström, 1973), requires usage of one of the criteria introduced by Boström (1973), [Al/(Al + Fe + Mn)] < 0.3, in addition to the ternary diagram by Bonatti et al. (1972). Bonatti (1981) revised the above ratio suggesting a slight correction: Al/(Al + Fe + Mn) < 0.4. In summary, we would suggest the use of the ternary diagram by Bonatti et al. (1972) in combination with Boström's (1973) ratio [Al/(Al + Fe + Mn)] < 0.3 for the identification of metalliferous sediments. At the same time, we are well aware that these quantitative criteria follow conventional use and that

any classification of submarine Fe–Mn deposits is limited by the common occurrence of transitional cases.

According to summary work (Boström, 1973; Gurvich, 2006) and our limited comparison (Table 7), it appears that metalliferous sediments might be differentiated in two groups: (1) ridge sediments blanketing ridge crests and flanks down to the CCD; and (2) deep sediments located beneath the CCD in the deeps near the mid-ocean ridges. The sediments from the first group are oozes and element concentrations in them need to be recalculated on an abiogenic basis in order to recognize them as metalliferous. The sediments in the second group are almost stripped of CaCO$_3$ even if they are located in a zone with prevailing calcareous plankton bioproduction in the euphotic layer.

According to the two criteria we suggest above, four of the studied samples are metalliferous: ##292, 293, 294 and 296-lower (Table 4 and Fig. 4). Sample #297-grey is a typical terrigenous sediment with high Al, Ti and Si contents (see Section 4). The other three samples (##296-upper, 297-light and 302) are close to be considered as metalliferous (Table 4). Three of the metalliferous samples (##292, 293 and 296-lower) are ridge metalliferous sediments, while the forth one (#294) is a typical deep metalliferous sediment, very similar to those in the Bauer Deep (Tables 4 and 6).

Silicon is an element with dual nature in the studied sediments: (1) detrital from the nearest landmass, South America; and (2) authigenic (hydrothermal or basaltic). No biogenic opal (diatoms, radiolarians) has been found. We have observed and identified aluminosilicates (possibly detrital) and amorphous silicates (Si–Al–Mg gel-like aggregates; possibly hydrothermal) during our SEM and XRD investigations. Although no basaltic glass shards were observed we cannot fully exclude their presence in the studied

Table 7

Comparison of chemical composition of H.M.S. *Challenger* (1872–1876) metalliferous sediments with composition of metalliferous sediments from similar settings.

Sample #	Location	Si (wt.%)	Ti	Al	Fe	Fe$_{CFB}$	Mn	Mn$_{CFB}$	Mg	Ca	Na	K	P	C$_{org}$	CaCO$_3$	Al/(Al + Fe + Mn)	Fe/ Mn	Ba (ppm)	Co	Cr	Cu	Hf	Mo	Ni	Pb	Sb	Sc	Sr	Th	V	Y	Zn	Zr
292[a]	PAR crest	0.67	0.01	0.14	2.40	13.2	0.94	5.20	0.23	37.9	0.15	0.03	0.07	1.28	81.9	0.04	2.55	1422	12.2	7.27	126	0.22	10.3	88.6	197	1.03	1.42	1335	0.54	72	28.4	68.3	26.4
293[a]	PAR flank	3.98	0.14	1.38	13.0	26.7	4.10	8.42	0.71	21.7	0.25	0.27	0.33	b.d.l.[f]	51.2	0.07	3.18	3583	62.2	10.3	839	2.61	95.1	635	76.8	7.04	7.70	1038	2.61	330	136	226	191
294[a]	SE Pacific Basin	13.5	0.28	4.16	20.5	20.5	5.39	5.40	1.69	1.6	0.93	1.28	0.52	0.23	0.01	0.14	3.80	10650	140	12.3	1498	6.59	157	1116	131	14.8	16.4	529	6.48	505	246	404	362
296-lower[a]	CR flank	9.53	0.20	3.19	6.08	11.1	1.66	3.03	0.94	21.2	0.66	0.80	0.16	0.59	45.2	0.29	3.67	6447	62.7	20.9	501	2.44	49.4	539	597	5.53	12.0	894	4.15	164	75.8	384	139
St. 1002[b]	PAR crest	–	0.02	0.25	1.40	25.00	0.51	9.11	–	–	–	–	–	–	94.4	0.12	2.75	1840	60	–	86	0.5	–	85	–	0.9	2.7	–	1.2	27	–	44	52
St. 999[b]	PAR flank	–	0.05	0.38	4.48	26.35	1.61	9.47	–	–	–	–	–	–	83.0	0.06	2.78	1700	190	–	134	2.0	–	250	–	4.0	5.4	–	1.8	135	–	140	210
St. 997[b]	SE Pacific Basin	–	0.30	4.25	17.25	17.25	5.32	5.32	–	–	–	–	–	–	0	0.16	3.24	5260	228	–	1520	8.4	–	1060	–	12	23	–	14	440	–	448	400
42°S[c]	PAR crest	1.11	–	0.28	4.59	17.65	1.56	6.00	0.41	29.3	–	0.07	–	–	74.0	0.04	2.94	1433	19	–	210	–	–	100	–	–	–	–	–	–	–	125	–
138-pilot[d]	Bauer Deep	15.35	–	2.23	21.68	21.9	5.45	5.5	2.47	–	0.64	0.94	–	–	1.0	0.08	3.98	15840	139	–	1267	–	–	1139	–	–	–	931	–	–	–	663	–
140-pilot[d]	Bauer Deep	19.35	–	3.38	14.41	14.7	3.77	3.85	2.60	–	0.73	1.18	–	–	2.0	0.16	3.82	19894	206	–	960	–	–	843	–	–	–	862	–	–	–	588	–
143-pilot[d]	Bauer Deep	19.35	–	1.45	10.88	11.1	4.51	4.6	1.51	–	0.62	0.60	–	–	2.0	0.09	2.41	16170	118	–	941	–	–	853	–	–	–	1009	–	–	–	470	–
Pelagic red clay[e]	Pacific	25.80	0.47	8.63	5.39	–	0.43	–	2.04	0.5	0.96	2.21	0.11	0.27	–	0.60	12.50	3900	113	64	230	–	10	210	34	–	25	710	–	117	150	165	–

[a] This study.

[b] Migdisov et al. (1979).

[c] Walter and Stoffers (1985).

[d] Sayles et al. (1975).

[e] Bischoff et al. (1979).

[f] b.d.l. = below detection limit.

sediments. In order to estimate the Si excess in our samples as a result of authigenic (hydrothermal or basaltic) input we have used its ratio to Al (a typical detrital element) in the terrigenous sample #297-grey (Si/Al = 2.81) as a background marker. The other sample from the same site, #297-light shows a slight Al excess (Si/Al = 2.69), while the Si/Al ratio of sample #296-upper (2.85) is very close to the background value. Obviously these two samples might be considered as terrigenous sediments. The metalliferous sediments (##292, 293, 294, 296-lower) and sample #302 have excess Si (Si/Al = 4.79, 2.88, 3.25, 2.99, 3.47, respectively), which clearly demonstrates authigenic Si input. Samples ##292 and 302 are close to ridge crests and basaltic contribution to their Si excess cannot be ruled out. Most probably, the other three metalliferous samples collected away from the ridge crests received their excess Si from a hydrothermal source (plume fallout) mainly.

5.2. Mineralogy of the metalliferous sediments

The abiogenic part of the studied metalliferous sediments is composed of poorly-crystalline, X-ray amorphous Fe–Mn-oxyhydroxides and Si–Al–Mg gels. Rare Fe–Mn micronodules scattered in these sediments suggest incipient diagenesis in the sediment (Dekov et al., 2003). The fairly constant magnetic parameters of the sediments when normalized to Fe content suggest a single source of magnetic minerals. The essential magnetic phases should be the Fe–Mn-oxyhydroxide precipitates, although a little contribution of volcaniclastic magnetite may be expected in sample #302 because of its close proximity to the active Chile Ridge (Fig. 1). It appears that the measured susceptibility (χ) is largely due to paramagnetic phases because the calculated paramagnetic susceptibility (χ_p) is 50–77% of the total χ (except for sample #302 where it is only 25%). The extra component of susceptibility is due to traces of soft ferrimagnetic minerals like magnetite or maghemite, as indicated in the following discussion. The negligible contribution of goethite (or hematite) is demonstrated by the low stability of IRM against AF: only 3–8% remains after treatment at 120 mT (IRM_{res} in Table 3). Hysteresis parameters of sample #294 [M_s = 61.5 mA m^2/kg, M_{rs}/M_s = 0.28, B_c = 15 mT, B_{cr} = 28 mT (Fig. 5)], point to pseudo-single domain magnetite/maghemite. Combining both non-paramagnetic susceptibility and IRM we estimated the amount of magnetite/maghemite as ≤0.1% wt., which explains why such phase was not detected by XRD (detection limits ~4%). The saturation magnetization of sample #294 is 1000 times less than the one of pure maghemite, which confirms this estimate. It is difficult to say whether this small amount of magnetite/maghemite is from extraterrestrial (micrometeorites contain ~10% magnetite on average, e.g., Suavet et al., 2009), volcaniclastic, or authigenic material. Since we did not find cosmic spherules in the magnetic sub-fraction of sample #294 we assume that, if present, the micrometeorites may be enclosed inside the black micronodules and crusts we observed (e.g., Murray and Renard, 1891). In summary, besides the paramagnetic signal of the X-ray amorphous Fe–Mn-oxyhydroxides, the magnetic survey revealed a minor amount (up to 0.1% in the most Fe-rich sample) of ferrimagnetic material,
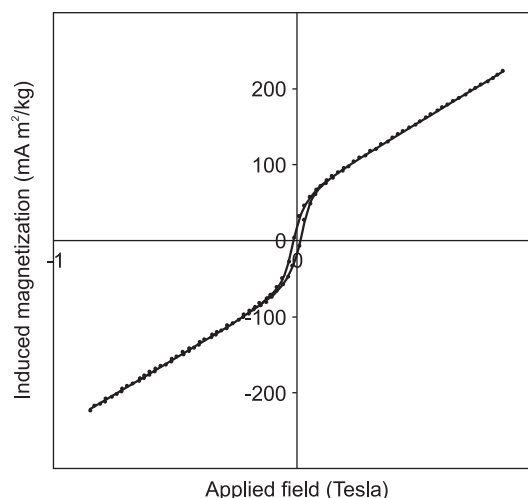

Fig. 5. Hysteresis loop measured on sample #294 (Micromag VSM; 0.12 g sample fragment).

likely micron-sized magnetite or maghemite, and a single source of magnetic material, according to the constant values of Fe-normalized magnetic parameters. No evidence for an extraterrestrial origin of these ferrimagnetic phases was found.

5.3. REE signature of the metalliferous sediments

The REE distribution patterns of the studied metalliferous sediments differ from that of the pelagic red clay (which has slightly positive Ce and negative Eu anomalies) and show some similarities with that of deep seawater from the southern Pacific (Fig. 3). This is a consequence of precipitation of Fe–Mn hydrothermal phases in close contact with seawater and corroborates the common knowledge that metalliferous sediments inherit their REE signature from the deep seawater (Dubinin, 2004). The less pronounced negative Ce anomaly than that of the seawater suggests a short residence time of the Fe–Mn precipitates in the hydrothermal plume and restricted (in time) contact with the ambient seawater. The weak positive or no Eu anomaly in some of the REE distribution patterns implies a hydrothermal imprint (positive Eu anomaly) that has been reduced or erased due to seawater influence (e.g., Stancin et al., 2008).

5.4. Pb, Sr and Nd isotope signatures of the metalliferous sediments

The *Challenger* metalliferous sediments were collected at the end of the 19th century (i.e., after the onset of the Industrial Revolution, but decades before the onset of leaded gasoline usage) therefore we must address anthropogenic and natural sources as possible contributors of Pb to the sediments. Anthropogenic Pb contamination could have happened during sample collection and storage. Samples were subjected to sequential leaching, therefore it is expected that any Pb contamination introduced during collection and/or storage, will be removed during the two

(1 M acetic, followed by 2 M HCl) leaching steps. ==In addition, anthropogenic Pb released in the atmosphere from ore smelting and/or fossil fuel combustion is accumulated in relatively soluble fractions and also will be removed during the leaching steps== (Hamelin et al., 1989; Teutsch et al., 2001). As our results show, pairs of leachates and residues (Table 5 and Fig. 6) overall have similar Pb isotopic characteristics, arguing against anthropogenic influence on the Pb isotope record of the metalliferous sediments collected during the H.M.S. *Challenger* expedition.

Natural Pb sources that can be important in the studied region include hydrothermal component derived from local Pacific MORB and/or Pacific seawater, and eolian component dominated by input from South America. Earlier work on metalliferous sediments from an EPR transect (DSDP Leg 92) showed a Pb isotopic signature that is best explained by mixing between seawater and basalt-derived Pb (Barrett et al., 1987). Lead isotope values from DSDP Leg 92 metalliferous sediments form an array extending
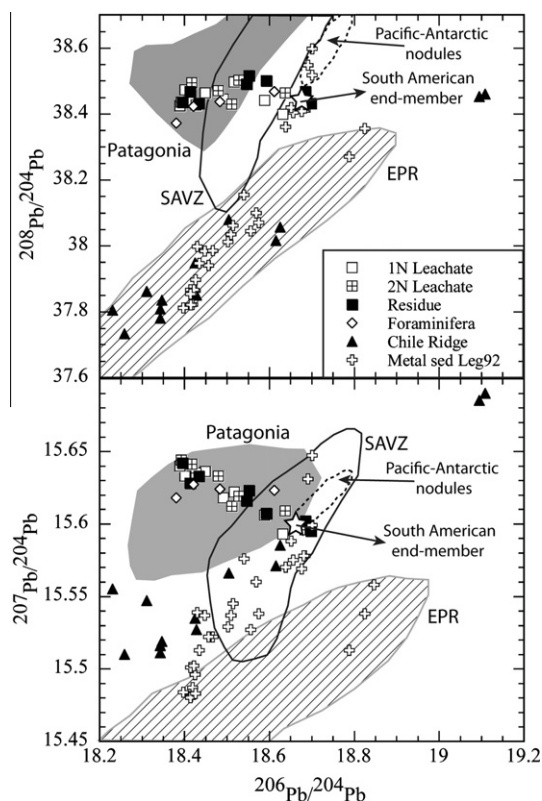
Fig. 6. Pb isotope data for possible sources for *Challenger* metalliferous sediments. Data for Chile Ridge, East Pacific Rise and South Andean Volcanic Zone (SAVZ) from GeoRoc database; Chile Ridge basalts from Bach et al. (1996); Patagonia from Gorring and Kay (2001); DSDP Leg 92 metalliferous sediments from Barrett et al. (1987); Pacific–Antarctic nodules (Circum–Antarctic Mn-nodules, Pacific side) from Abouchami and Goldstein (1995); and South American sedimentary end-member from Stancin et al. (2006). Note, that *Challenger* samples show distinct Pb isotopic compositions from EPR and CR and plot entirely in the fields of SAVZ and Patagonia, presumably the sources of eolian material to the studied part of the Pacific. For more discussion see the text.

from the EPR field to more-radiogenic values, presumably corresponding to Pacific seawater in the region (Fig. 6). In contrast, *Challenger* metalliferous sediments form a linear trend that is perpendicular to that of the DSDP Leg 92 data. The linear trend formed by Challenger data can be indicative of involvement of two end-members, however, we cannot identify clearly two distinct sources that can explain the array. There are several potential candidates for the high $^{206}Pb/^{204}Pb$ source, including the "South American end-member" defined by Stancin et al. (2006), Pacific–Antarctic component, represented by the Pacific–Antarctic nodules field (Abouchami and Goldstein, 1995), and the most radiogenic end of the Chile Ridge MORB field (Fig. 6). Overall, *Challenger* data are very distinct from EPR and CR MORB, indicating no significant Pb contribution from local basaltic sources. The Pacific–Antarctic nodules field show overall higher $^{206}Pb/^{204}Pb$, $^{207}Pb/^{204}Pb$, and $^{208}Pb/^{204}Pb$ compared to the *Challenger* samples (Fig. 6). The *Challenger* sediments isotopic values extend from the South American end-member to higher $^{207}Pb/^{204}Pb$ and lower $^{206}Pb/^{204}Pb$ (Fig. 6) and plot entirely in the Pb isotopic fields for Neogene plateau lavas in Patagonia (Southern Argentina) and the South Andean Volcanic Zone (SAVZ). The latter indicates that aeolian input by the westerlies from South America controls the Pb isotopic composition of the studied metalliferous sediments. The lack of significant Pb input from Pacific MORB is in contrast with the previous findings for metalliferous sediments from DSDP Leg 92 (Barrett et al., 1987). Settling hydrothermal plume particles scavenge a number of trace metals, including Pb, from the ambient seawater and recent work by Kamenov et al. (2009) showed that Pb in Mediterranean low-temperature hydrothermal deposits is controlled by seawater Pb, which itself is controlled by atmospheric input. Furthermore, Jones et al. (2000) showed that eolian input significantly impacts the Pacific seawater Pb budget. Clearly the aeolian material derived from South America is the main source for the aluminosilicate component (the residues) observed in the *Challenger* sediments. The latter is also supported by the residues in Sr–Nd isotopic systematics, as described below. Apparently, the soluble Pb in the regional seawater that was scavenged by the settling hydrothermal plume particles, was also controlled by the regional eolian input from South America. The latter is evident in the fact that Pb isotope data of the leachates also plot within the Patagonia-SAVZ fields (Fig. 6).

Sr and Nd data from the *Challenger* metalliferous sediments (leachates and residues) also plot within the Patagonia-SAVZ field (Fig. 7), further supporting derivation from the South American sources. At the same time, however, there is a clear seawater contribution to the Sr isotopic record. Most of the 1 M acetic acid leachates have $^{87}Sr/^{86}Sr$ very similar to modern seawater, indicating that Sr was contributed by the latter in the leachable fraction (Fig. 7). Residues, on the other hand, show quite variable Sr isotopic compositions, mostly less radiogenic than modern seawater, consistent with derivation of the residual aluminosilicate fraction from South American sources (Fig. 7). Note that the residues form an array towards the EPR-CR (Fig. 7), which is consistent with the subduction
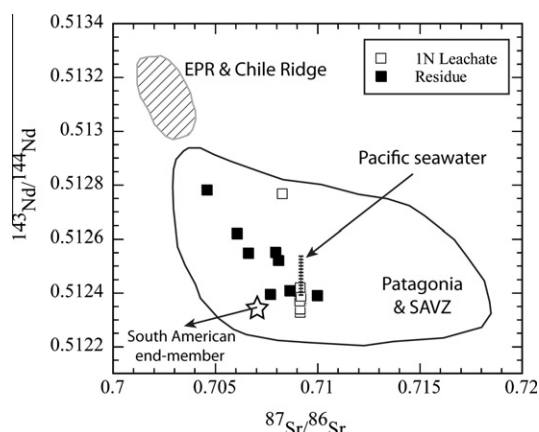
Fig. 7. Sr–Nd isotope data for possible sources for *Challenger* metalliferous sediments. Data sources same as in Fig. 6. Pacific seawater Nd isotopic range after Frank (2002). Note that *Challenger* metalliferous sediments (leachates and residues) plot in the field of Patagonia and SAVZ and that even the 1 M acetic acid leachates Nd isotopic compositions cannot be solely explained by Pacific seawater. Note also that the residues form a trend toward the EPR/Chile Ridge field. This trend cannot be explained by hydrothermal contribution from EPR/Chile Ridge as the residues represent the alumosilicate (detrital) fraction of the sediments. The trend simply reflects the subduction processes along the western margin of South America that ultimately generated the isotopic signal observed in the Patagonia-SAVZ. For more discussion see the text.

nature of the volcanism along the Andean margin of South America. Some of the leachable fractions of the sediments (Fig. 7) show $^{143}Nd/^{144}Nd$ ratios that overlap with the known range for Pacific seawater (Frank, 2002). The latter indicates that some of the Nd may have been derived from the Pacific seawater.

5.5. Fe and Zn isotope signatures of the metalliferous sediments

We investigated Fe–Zn-isotope systems in two basalt samples (divided into four subsamples) along with the metalliferous sediments (see Section 3.1) aiming at obtaining an insight into Fe and Zn isotope fractionation during the processes of basalt alteration and precipitation of metalliferous sediment. Therefore we need to know the nature of the basalt subsamples before discussing the isotope fractionation processes. In this respect we will use some basic geochemical data without intending a thorough discussion of the basalt petrochemistry since this is not the purpose of our study.

The weakly altered basalt (SO 40-38D/1) is slightly enriched in Al relative to the fresh basalt (Table 6) and this is not surprising given that Al is immobile during basalt alteration (hydrothermal or seafloor weathering) and remains in the basalt which causes its passive enrichment. The enrichment in Fe and, especially in Zn, of this sample (Table 6) is unexpected since both elements are mobile and likely to be leached away during basalt alteration. However, these data can be explained by the location of this sample.

It was taken close to a crack which implies that re-precipitation of leached Fe and Zn may have taken place along the crack walls. The other two subsamples (SO 40-38D/2 and SO 40-38D/3) are very rich in Fe and Zn, and substantially depleted in Al (Table 6), which cannot be easily explained by basalt alteration processes. Even though the low Al content may be explained by the high Fe concentrations causing Al "dilution", the large EFs suggest that input of additional Fe and Mn (9.12 and 7.35 wt.%, respectively; not in Table 6) rather than basalt alteration alone have played a key role in the formation of these samples. Two principal types of processes may have supplied Fe and Mn (and related trace elements) to the surface of the basalt: hydrothermal and hydrogenetic. In order to differentiate their possible contribution to the composition of these two subsamples we used the ternary diagram by Bonatti et al. (1972) (Fig. 4). Based on this plot we may conclude that hydrogenetic processes have played an appreciable role in the formation of the red, hard surface of altered basalt (SO 40-38D/2), while the red, soft precipitate on altered basalt (SO 40-38D/3) can be considered as a metalliferous sediment precipitated in the vicinity of active hydrothermal vents. Its Al/(Al + Fe + Mn) ratio (0.11) also supports this assumption.

The Fe isotope data show that the H.M.S. *Challenger* metalliferous sediments are clearly lighter than the basalt (Fig. 8A). The fresh and slightly altered basalt have the same isotopic value, indicating that the alteration is very slight indeed. The $\delta^{56}Fe$ values for both the red, hard surface of altered basalt and the red, soft precipitate on altered basalt are very close to those of the metalliferous sediments (Fig. 8A), which corroborates that the former materials are dominated by FeOOH precipitates and that there is no strongly altered basalt in our basalt-related samples, as initially believed (see Section 3.1). Our $\delta^{56}Fe$ data fit the previously reported results that hydrothermal leaching of igneous rocks ($\delta^{56}Fe$ ~0.1‰) produces a hydrothermal fluid of lighter Fe composition ($\delta^{56}Fe$ ~−0.6 to 0‰; Anbar and Rouxel, 2007).

The isotopes of dissolved Fe in the hydrothermal fluid can suffer fractionation from several inorganic processes. The most dramatic fractionation occurs by formation of Fe-sulfides, which particles grow quickly and precipitate from the hydrothermal plume (Severmann et al., 2004). This process enriches the hydrothermal plume in the lighter Fe component (Johnson et al., 2008). The $\delta^{56}Fe$ values for FeOOH precipitated on the basalt (samples SO 40-38D/2 and SO 40-38D/3), presumably near the hydrothermal vents (Fig. 8A), are similar to those of the metalliferous sediments away from the ridge, which indicates no sulfide-driven fractionation in the hydrothermal plume and probably a large Fe/H_2S ratio in the fluids (e.g., Severmann et al., 2004).

Fe oxidation also causes fractionation, with lighter isotopes being enriched in the Fe^{2+} fraction (Severmann et al., 2003). The actual effect of this fractionation depends on the oxygen concentration in seawater and the rapidity of mixing with the hydrothermal fluids, which affect the Fe oxidation rate. Such rate varies across active ridges in the several oceans, and the time in which complete oxidation
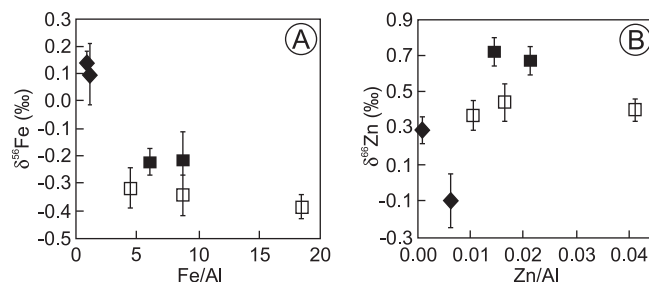
Fig. 8. Fe isotope composition *vs.* Fe/Al ratios (A) and Zn isotope composition vs. Zn/Al ratios (B) for studied metalliferous sediments and basalt samples. Closed diamonds = fresh (SO 40-31D) and yellowish altered basalt (SO 40-38D/1); closed squares = red, hard surface of altered basalt (SO 40-38D/2) and red, soft precipitate on altered basalt (SO 40-38D/3); open squares = distal metalliferous sediments (##292, 293, 294).

is achieved varies from minutes to hours (Statham et al., 2005). Slow oxidation produces fractionation within the hydrothermal plume as Fe^{3+} starts to precipitate as FeO-OH and the corresponding isotopically heavier fraction is retrieved from the plume. Fast oxidation precludes such effect. Our samples show a possible small difference of $\delta^{56}Fe$ (0.10–0.17‰) between the precipitates on the basalt and metalliferous sediments formed away from the ridge (Table 6 and Fig. 8A), which might be produced by relatively slow Fe oxidation. Statham et al. (2005) indicate that the Fe oxidation rate in the EPR area results in a mean Fe^{2+} half-life of 2.31 ± 0.23 h, and 99% oxidation occurs after 16.23 h. Further to this, fractionation in the plume depends on the velocity of particle sedimentation, velocity of the currents, topography, etc. The minimum distance of any of the sites of collection of our metalliferous sediments to a known active hydrothermal site is ~110 km (Fig. 1), which is ~100 times the calculated lateral distance travelled by the plume before all Fe is oxidized at the EPR area (Statham et al., 2005). Our data are thus consistent with a slow Fe oxidation rate at EPR that caused a small Fe fractionation during oxidation (99% oxidation completed ~1.2 km from the plume source) and deposition of the heavier Fe as FeOOH (heavier Fe is more abundant towards the plume source).

The $\delta^{66}Zn$ value for the fresh basalt (Table 6 and Fig. 8B) is within the range most frequently reported (0.2–0.35‰; Chapman et al., 2006; Cloquet et al., 2007). The slightly altered basalt (SO 40-38D/1), however, appears to be problematic because: (1) it is enriched in Zn with respect to the fresh basalt; and (2) Zn is enriched in lighter isotopes. None of these processes is expected from simple leaching, as Zn should be preferentially leached away, and leaching likely result in loss, even if very small, of the lighter isotopes as observed for other d-block elements like Fe (Cloquet et al., 2007; Chapman et al., 2009). These data can be explained by *in situ*, within the rock, precipitation of a Zn phase from fluid circulating through the basalt and where Zn is derived from basalt leaching. In other words, the point of sampling might correspond to a place where some secondary precipitation occurred as concluded before (see paragraph #2 of Section 5.5). The precipitated phase is likely a sulfide, which would explain both the higher Zn concentration and the lighter Zn isotopes: precipitated Zn in non-equilibrium conditions would be lighter than the dis-

solved one (Mason et al., 2005; Cloquet et al., 2007; John et al., 2008).

The $\delta^{66}Zn$ values are more positive for the FeOOH precipitates that were deposited on the basalt (samples SO 40-38D/2 and SO 40-38D/3) than for the H.M.S. *Challenger* metalliferous sediments deposited away from the ridges (Fig. 8B). The likely mechanism for the retention of Zn in the metalliferous sediments is adsorption on FeOOH (Gurvich, 2006). Such process has been documented to concentrate heavier isotopes (Pokrovsky et al., 2005; Cloquet et al., 2007; Balistrieri et al., 2008; Juillot et al., 2008), explaining that all these samples have higher $\delta^{66}Zn$ values than the basalt. It is generally observed that most Zn dissolved in the hydrothermal fluids precipitates as sulfide below the seafloor and in the proximity of the hydrothermal vents (e.g., Edmonds and German, 2004). Therefore it is expected that Zn in the distal metalliferous sediments is contributed by seawater. However, the $\delta^{66}Zn$ values of the three *Challenger* metalliferous sediment samples do not support a seawater contribution only. John et al. (2005) have measured the value $\delta^{66}Zn$ = +0.46‰ for deep Pacific seawater. This value is slightly more positive than the one of our distal sediments although still within the ±2σ range (Fig. 8B). Zinc adsorbed on FeOOH from such ambient seawater alone should have been enriched in heavier isotopes, with $\delta^{66}Zn$ > +0.46‰. In fact, $\delta^{66}Zn$ values at the surface of hydrogenous Fe–Mn nodules at similar latitudes are 0.74–1.16‰ (Albarède, 2004), significantly higher than our values. We propose that the $\delta^{66}Zn$ signature from seawater was altered towards lighter values by the following contributions.

Hydrothermal Zn may have escaped removal by precipitation, as acknowledged possible in some instances (John et al., 2008). The extent of such removal is a function of the ratio (Fe + chalcophile metals)/H_2S, and there is evidence from Fe isotope data that Fe/H_2S is low. Thus, the Zn that did not precipitate as sulfide, would have been progressively removed by adsorption on FeOOH particles along the path of the non-buoyant plume, which resulted in a progressive fractionation with the lighter fraction travelling farther and suffering deposition later by the same adsorption process. At sufficient distance from the vent, this hydrothermal Zn would be lighter than that in the background seawater. Another source of light Zn, although evidently small, is the minor detrital aluminosilicate minerals
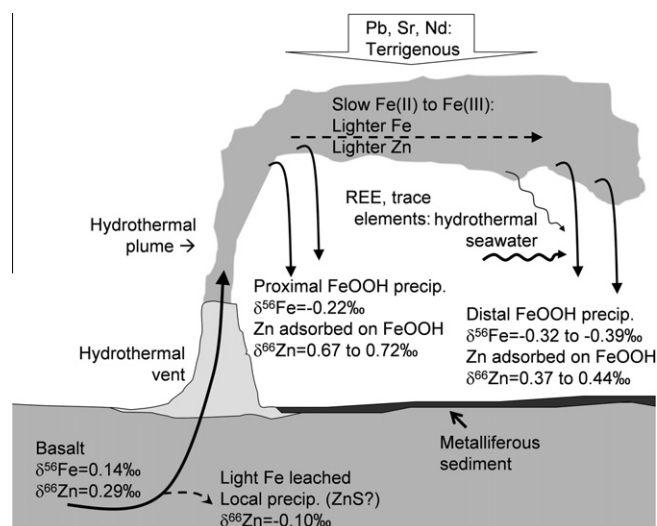
Fig. 9. Summary sketch of the processes producing the chemical and isotope signature of the metalliferous sediments. The wavy arrows indicate the relative input of REE and trace elements in the metalliferous sediment, greater from seawater than from the hydrothermal fluids.

(Table 2) with probable $\delta^{66}Zn$ values 0.17–0.35 (Albarède, 2004) and barite, which, if precipitated in non-equilibrium conditions, would be enriched in light Zn as discussed above. Finally, our magnetic mineralogy studies (Section 5.2) revealed up to 0.1% of ferrimagnetic material (magnetite or maghemite) of probably basaltic origin in the distal sediments. Spinel (magnetite included) is the fourth most abundant mineral in the MORB (Hekinian, 1982). This means we may assume that the distal metalliferous sediments we have studied contain a few percent of basaltic material (glass, olivine, plagioclase, pyroxene and spinel), with $\delta^{66}Zn$ ~0.3‰ (Table 6). Indeed, fine-grained basaltic material (often altered) is a common minor constituent of this type of metalliferous sediments (Gurvich, 2006). All these three contributions may have decreased the overall Zn isotope signature and reduced the influence of seawater $\delta^{66}Zn$ scavenged by the FeOOH component in our distal sediments.

6. CONCLUSIONS

The *Challenger* metalliferous sediments are of two types (according to their location and composition): (1) ridge sediments blanketing ridge crests and flanks down to the CCD (oozes); and (2) deep sediments located beneath the CCD in the deeps near the mid-ocean ridges (stripped of $CaCO_3$). The abiogenic part of these metalliferous sediments is composed mainly of poorly-crystalline to X-ray amorphous Fe–Mn-oxyhydroxides (possibly goethite, δ-MnO_2), and another amorphous silicate (Si–Al–Mg[–Fe] gels?) phase. Mineral phases of terrigenous origin, as kaolinite, mica, quartz and plagioclase, appear in varying concentration depending on proximity to the landmasses. The *Challenger* metalliferous sediments have similar geochemical features: very high Fe and Mn content (on carbonate-free basis), very low Al/(Al + Fe + Mn), and high content (on carbonate-free basis) of As, Ba, Be, Bi, Cd, Co, Cu, Mo, Ni, Pb,

Sb, Th, Tl, U, V, W, Y, Zn, Zr. Their REE distribution patterns are, in general, similar to that of deep seawater and show weak signs of hydrothermal imprint (weak positive or no Eu anomaly). This suggest precipitation of hydrothermal phases (oxyhydroxides and silicates) during mixing of hydrothermal fluid with ambient seawater in such proportions that the seawater negative Eu anomaly has reduced the original high positive Eu anomaly of the fluid. The residence time of the hydrothermal precipitates in the hydrothermal plume also has impact on the final REE distribution pattern.

Overall, our trace element and isotope data are consistent with the following model for formation of the *Challenger* metalliferous sediments (Fig. 9). Sr, Nd, and Pb isotopes of the *Challenger* metalliferous sediments show that any original MORB signal on these isotopes is more or less completely obliterated by seawater and/or terrigenous input. The Pb isotopic compositions of the sediment samples indicate that Pb was mainly controlled by terrigenous input from South American sources. Most probably, aeolian input from South America contributed the dissolved Pb to regional seawater as reflected in the leachate compositions. This dissolved Pb was scavenged on the FeOOH particulates and subsequently incorporated in the metalliferous sediments. The Pb isotopic compositions of the residual alumosilicate phase of the sediments also reflect terrigenous input from South America. Sr and Nd isotopes of the leachate phase mainly reflect seawater contribution, whereas the Sr and Nd isotopes of the alumosilicate residue are consistent with aeolian input from South America. Iron isotopes indicate relatively slow Fe^{2+} to Fe^{3+} oxidation in the non-buoyant plume, thus producing relatively lighter Fe isotopic signature in the FeOOH particles that formed the *Challenger* metalliferous sediments. The newly formed FeOOH particles scavenged Pb, Sr, Zn, REE, and by analogy a number of other trace metals from the ambient seawater, although other sources of Zn are necessary,

potentially hydrothermal fluid and detrital aluminosilicates, barite and volcanic glass. The accumulation of these FeO-OH particles eventually formed the distal metalliferous sediments collected during the *Challenger* expedition.

ACKNOWLEDGMENTS

REFERENCES

Abouchami W. and Goldstein S. L. (1995) A lead isotopic study of Circum–Antarctic manganese nodules. *Geochim. Cosmochim. Acta* **59**, 1809–1820.

Albarède F. (2004) The stable isotope geochemistry of copper and zinc. *Rev. Mineral. Geochem.* **55**, 409–427.

Anbar A. D. and Rouxel O. (2007) Metal stable isotopes in Palaeoceanography. *Annu. Rev. Earth Planet. Sci.* **35**, 717–746.

Arnold T., Harvey J. N. and Weiss D. J. (2008) An experimental and theoretical investigation into the use of H_2 for the simultaneous removal of ArO+ and ArOH+ isobaric interferences during Fe isotope ratio analysis with MC-ICP-MS. *Spectrochim. Acta Part B* **63**, 666–672.

Bach W., Erzinger J., Dosso L., Bollinger C., Bougault H., Etoubleau J. and Sauerwein J. (1996) Unusually large Nb–Ta depletions in North Chile ridge basalts at 36°50′ to 38°56′S: major element, trace element, and isotopic data. *Earth Planet. Sci. Lett.* **142**, 223–240.

Balistrieri L. S., Borrok D. M., Wanty R. B. and Ridley W. I. (2008) Fractionation of Cu and Zn isotopes during adsorption onto amorphous Fe(III) oxyhydroxide: experimental mixing of acid rock drainage and ambient river water. *Geochim. Cosmochim. Acta* **72**, 311–328.

Baker E. T., Hey R. N., Lupton J. E., Resing J. A., Feely R. A., Gharib J. J., Massoth G. J., Sansone F. J., Kleinrock M., Martinez F., Naar D. F., Rodrigo C., Bohnenstiehl D. and Pardee D. (2002) Hydrothermal venting along Earth's fastest spreading center: East Pacific Rise, 27.5°–32.3°S. *J. Geophys. Res.* **107**(B7). doi:10.1029/2001JB000651.

Barrett T. J., Taylor P. N. and Lugowski J. (1987) Metalliferous sediments from DSDP Leg 92: the East Pacific Rise transect. *Geochim. Cosmochim. Acta* **51**, 2241–2253.

Bird R. T., Naar D. F., Larson R. L., Searle R. C. and Scotese C. R. (1998) Plate tectonic reconstructions of the Juan Fernandez microplate: transformation from internal shear to rigid rotation. *J. Geophys. Res.* **103**, 7049–7067.

Bird R. T., Tebbens S. F., Kleinrock M. C. and Naar D. F. (1999) Episodic triple-junction migration by rift propagation and microplates. *Geology* **27**, 911–914.

Bischoff J. L., Heath G. R. and Leinen M. L. (1979) Geochemistry of deep-sea sediments from the Pacific Manganese Nodule Province. DOMES Sites A, B, and C. In *Marine Geology and Oceanography of the Pacific Manganese Nodule Province* (eds. J. L. Bischoff and D. Z. Piper). Plenum Press, NY, pp. 397–436.

Bonatti E. (1981) Metal deposits in the oceanic lithosphere. In *The Sea*, vol. 7 (ed. C. Emiliani), pp. 639–686. The Sea. John Willey and Sons, NY.

Bonatti E., Kraemer T. and Rydell H. (1972) Classification and genesis of submarine iron–manganese deposits. In *Ferromanganese Deposits of the Ocean Floor* (ed. D. R. Horn). Arden House, Harriman, NY, pp. 149–166.

Boström K. (1973) The origin and fate of ferromanganoan active ridge sediments. *Stockholm Contrib. Geol.* **27**, 149–243.

Chapman J., Mason T. F. D., Weiss D. J., Coles B. J. and Wilkinson J. J. (2006) Chemical separation and isotopic variations of Cu and Zn from five geological reference material. *Geostand. Geoanal. Res.* **30**, 5–16.

Chapman J. B., Weiss D. J., Shan Y. and Lemberger M. (2009) Iron isotope fractionation during leaching of granite and basalt by hydrochloric and oxalic acids. *Geochim. Cosmochim. Acta* **73**, 1312–1324.

Cloquet C., Carignan J., Lehmann M. F. and Vanhaecke F. (2007) Variation in the isotopic composition of zinc in the natural environment and the use of zinc isotopes in biogeosciences: a review. *Anal. Bioanal. Chem.*. doi:10.1007/s00216-007-1635-y.

Corliss J. B., Dymond J., Gordon L. I., Edmond J. M., von Herzen R. P., Ballard R. D., Green K., Williams D., Bainbridge A., Crane K. and van Andel T. H. (1979) Submarine thermal springs on the Galapagos Rift. *Science* **203**, 1073–1083.

de Baar H. J. W., Bacon M. P., Brewer P. G. and Bruland K. W. (1985) Rare earth elements in the Pacific and Atlantic Oceans. *Geochim. Cosmochim. Acta* **49**, 1943–1959.

Dekov V. M., Marchig V., Rajta I. and Uzonyi I. (2003) Fe–Mn micronodules born in the metalliferous sediments of two spreading centers: East Pacific Rise and Mid-Atlantic Ridge. *Mar. Geol.* **199**, 101–121.

Dekov V. M., Kamenov G. D., Savelli C., Stummeyer J., Thiry M., Shanks W. C., Willingham A. L., Boycheva T. B., Rochette P., Kuzmann E., Fortin D. and Vértes A. (2009) Metalliferous sediments from Eolo Seamount (Tyrrhenian Sea): hydrothermal deposition and re-deposition in a zone of oxygen depletion. *Chem. Geol.* **264**, 347–363.

Dubinin A. V. (2004) Geochemistry of rare earth elements in the ocean. *Lithol. Mineral Resources* **39**, 289–307.

Edmonds H. and German C. R. (2004) Particle geochemistry in the Rainbow hydrothermal plume, Mid-Atlantic Ridge. *Geochim. Cosmochim. Acta* **68**, 759–772.

Frank M. (2002) Radiogenic isotopes: tracers of past ocean circulation and erosional input. *Rev. Geophys.* **40**, 1001. doi:10.1029/2000RG000094.

German C. R. and Von Damm K. L. (2006) Hydrothermal processes. In *The Oceans and Marine Geochemistry. Treatise on Geochemistry*, vol. 6 (ed. H. Elderfield), pp. 181–222.

Gorring M. L. and Kay S. M. (2001) Mantle processes and sources of Neogene slab window magmas from Southern Patagonia, Argentina. *J. Petrol.* **42**, 1067–1094.

Gurvich E. G. (2006). *Metalliferous Sediments of World Ocean. Fundamental Theory of Deep-Sea Hydrothermal Sedimentation.* Springer, Heidelberg.

Hamelin B., Grousset F., Biscaye P. E. and Zindler A. (1989) Lead isotopes Trade Wind aerosols at Barbados: the influence of European emissions over North Atlantic. *J. Geophys. Res.* **94**, 16243–16250.

Hannington M. D. and Jonasson I. R. (1992) Fe and Mn oxides at seafloor hydrothermal vents. In *Biomineralization Processes of Iron and Manganese* (eds. H. C. W. Skinner and R. W. Fitzpatrick). Catena, vol. 21, pp. 351–370.

Hekinian R. (1982). *Petrology of the Ocean Floor*. Elsevier Oceanography Series vol. 33. Elsevier, Amsterdam.

Hey R., Baker E., Bohnenstiel D., Massoth G., Kleinrock M., Martinez F., Naar D., Pardee D., Lupton J., Feely R., Gharib J., Resing J., Rodrigo C., Sansone F. and Walker S. (2004) Tectonic/volcanic segmentation and controls on hydrothermal venting along Earth's fastest seafloor spreading system, EPR 27°–32°S. *Geochem. Geophys. Geosyst.* **5**, Q12007. doi:10.1029/2004GC000764.

John S. G., Bergquist B. A., Saito M. A. and Boyle E. A. (2005) Zinc isotope variations in phytoplankton and seawater. *Geochim. Cosmochim. Acta* **69**, A546.

John S. G., Rouxel O. J., Craddock P. R., Engwall A. M. and Boyle E. A. (2008) Zinc stable isotopes in seafloor hydrothermal vent fluids and chimneys. *Earth Planet. Sci. Lett.* **269**, 17–28.

Johnson C. M., Beard B. L. and Roden E. E. (2008) The iron isotope fingerprints of redox and biogeochemical cycling in modern and ancient Earth. *Annu. Rev. Earth Planet. Sci. Lett.* **36**, 457–493.

Jones C. E., Halliday A. N., Rea D. K. and Owen R. M. (2000) Eolian inputs of lead to the North Pacific. *Geochim. Cosmochim. Acta* **64**, 1405–1416.

Juillot F., Marechal C., Ponthieu M., Cacaly S., Morin G., Benedetti M., Hazemann J. L., Proux O. and Guyot F. (2008) Zn isotope fractionation caused by sorption on goethite and 2-lines ferrihydrite. *Geochim. Cosmochim. Acta* **72**, 4886–4900.

Kamenov G. D., Dekov V. M., Willingham A. L., Savelli C. and Belluci L. G. (2009) Anthropogenic Pb in recent hydrothermal sediments from the Tyrrhenian Sea: implications for seawater Pb control on low-temperature hydrothermal systems. *Geology* **37**, 111–114.

Kamenov G. D., Perfit M. R., Mueller P. A. and Jonasson I. R. (2008) Controls on magmatism in an island arc environment: study of lavas and sub-arc xenoliths from the Tabar–Lihir–Tanga–Feni island chain, Papua New Guinea. *Contrib. Mineral. Petrol.* **155**, 635–656.

Lisitzin A. P., Bogdanov Yu. A., Murdmaa I. O., Serova V. V., Zverinskaya I. B., Lebedev A. I., Lukashin V. N. and Gordeev V. V. (1976) Metalliferous sediments and their genesis. In *Geological and Geophysical Research in South-East Pacific* (ed. A. P. Lisitzin). Nauka, Moscow, pp. 289–379 (in Russian).

Lonsdale P. (1976) Abyssal circulation of the southeastern Pacific and some geological implications. *J. Geophys. Res.* **81**, 1163–1176.

Marchig V. (1978) Brown clays from the Central Pacific–metalliferous sediments or not? *Geol. Jb. D* **30**, 3–25.

Marienfeld P. and Marchig V. (1992) Indications of hydrothermal activity at the Chile Ridge spreading centre. *Mar. Geol.* **105**, 241–252.

Mason T. F. D., Weiss D. J., Chapman J. B., Wilkinson J. J., Tessalina S. G., Spiro B., Horstwood M. S. A., Spratt J. and Coles B. J. (2005) Zn and Cu isotopic variability in the Alexandrinka volcanic-hosted massive sulphide (VHMS) ore deposit, Urals, Russia. *Chem. Geol.* **221**, 170–187.

Migdisov A. A., Bogdanov Yu. A., Lissitzin A. P., Gurvich E. G., Lebedev A. I., Lukashin V. N., Gordeev V. V., Girin Yu. P. and Sokolova E. G. (1979) Geochemistry of metalliferous sediments. In *Metalliferous Sediments of South-East Pacific Ocean* (ed. V. I. Smirnov). Nauka, Moscow, pp. 122–200.

Mills R. A. and Elderfield H. (1995) Hydrothermal activity and the geochemistry of metalliferous sediment. *Geophys. Monogr., AGU* **91**, 392–407.

Mullane E., Russell S. S., Gounelle M., Din V., Mason T. F. D., Weiss D. J. and Coles B. (2003) Precise and accurate determination of iron isotopes by multi-collector mass spectrometry. In *Plasma Source Mass Spectrometry: Applications and Emerging Technologies* (eds. G. Holland and S. D. Tanner). RSC, Cambridge, pp. 351–361.

Murray J. and Irvine R. (1895) On the manganese oxides and manganese nodules in marine deposits. *Trans. Roy. Soc. Edinburgh* **37**, 721–742.

Murray J. and Renard A. F. (1891) *Report on Deep-sea Deposits based on the Specimens Collected during the Voyage of H.M.S. Challenger in the Years 1872–1876*. Neill and Company, Edinburgh.

Nielsen S. H. H., Hodell D. A., Kamenov G. D., Guilderson T. and Perfit M. R. (2007) Origin and significance of ice rafted detritus in the Atlantic sector of the Southern Ocean. *Geochem. Geophys. Geosyst.* **Q12005**. doi:10.1029/2007GC001618.

Pokrovsky O. S., Viers J. and Freydier R. (2005) Zinc stable isotope fractionation during its adsorption on oxides and hydroxides. *J. Colloid Interface Sci.* **291**, 192–200.

Rochette P. and Lamarche G. (1986) Evolution des propriétés magnétiques lors des transformations minérales dans les roches: exemple du Jurassique Dauphinois (Alpes françaises). *Bull. Minér.* **109**(6), 687–696.

Rona P. A. (2008) The changing vision of marine minerals. *Ore Geol. Rev.* **33**, 618–666.

Sayles F. L., Ku T.-L. and Bowker P. C. (1975) Chemistry of ferromanganoan sediment of the Bauer Deep. *Geol. Soc. Amer. Bull.* **86**, 1423–1431.

Severmann S., German C. R., Edmonds H. N., Beard B. L. and Johnson C. M. (2003) The modification of hydrothermal Fe-isotopic signature during plume processes. *Geochim. Cosmochim. Acta* **67**, A424.

Severmann S., Johnson C. M., Beard B. L., German C. R., Edmonds H. N., Chiba H. and Green D. R. H. (2004) The effect of plume processes on the Fe isotope composition of hydrothermally derived Fe in the deep ocean as inferred from the Rainbow vent site, Mid-Atlantic Ridge, 36°14′N. *Earth Planet. Sci. Lett.* **225**, 63–76.

Siebert C., Nägler F. and Kramers J. D. (2001) Determination of molybdenum isotope fractionation by double-spike multicollector inductively coupled plasma mass spectrometry. *Geochem. Geophys. Geosyst.* **2**, paper number 2000GC000124.

Stancin A. M., Gleason J. D., Rea D. K., Owen R. M., Moore, Jr., T. C., Blum J. D. and Hovan S. A. (2006) Radiogenic isotopic mapping of late Cenozoic eolian and hemipelagic sediment distribution in the east-central Pacific. *Earth Planet. Sci. Lett.* **248**, 840–850.

Stancin A. M., Gleason J. D., Owen R. M., Rea D. K. and Blum J. D. (2008) Piston core record of Late Paleogene (31 Ma) to recent seafloor hydrothermal activity in the Southwest Pacific Basin. *Paleoceanography* **23**, PA1212. doi:10.1029/2006PA001406.

Statham P. J., German C. R. and Connelly D. P. (2005) Iron (II) distribution and oxidation kinetics in hydrothermal plumes at the Kairei and Edmond vent sites, Indian Ocean. *Earth Planet. Sci. Lett.* **236**, 588–596.

Stoffers P., Worthington T., Hekinian R., Petersen S., Hannington M., Türkay M., Ackermand D., Borowski C., Dankert S., Fretzdorff S., Haase K., Hoppe A., Jonasson I., Kuhn T., Lancaster R., Monecke T., Renno A., Stecher J. and Weiershäuser L. (2002) Widespread silicic volcanism and hydrothermal activity on the northern Pacific–Antarctic Ridge. *InterRidge News* **11**, 30–32.

Strahov N. M. (1976) *Geochemical Problems of Recent Oceanic Lithogenesis*. Nauka, Moscow.

Suavet C., Gattacceca J., Rochette P., Folco L., Perchiazzi N., Duprat J. and Harvey R. P. (2009) Magnetic properties of micrometeorites. *J. Geophys. Res.* **114**, B04102. doi:10.1029/2008JB005831.

Sun S.-S. and McDonough W. F. (1989) Chemical and isotopic systematics of oceanic basalts: implications for mantle composition and processes. In *Magmatism in the Ocean Basins*, vol. 42

(eds. A. D. Saunders and M. J. Norry), pp. 313–345. Magmatism in the Ocean Basins. Geological Society of London, Special Publications.

Tebbens S. F. and Cande S. C. (1997) Southeast Pacific tectonic evolution from early oligocene to present. *J. Geophys. Res.* **102**(B6), 12061–12084.

Teng F.-Z., Dauphas N. and Helz R. T. (2008) Iron isotope fractionation during magmatic differentiation in Kilauea Iki lava lake. *Science* **320**, 1620–1622.

Teutsch N., Erel Y., Halicz L. and Banin A. (2001) Distribution of natural and anthropogenic lead in Mediterranean soils. *Geochim. Cosmochim. Acta* **65**, 2853–2864.

Thompson M. and Walsh J. N. (2003) *Handbook of Inductively Coupled Plasma Atomic Emission Spectrometry*. Viridian, Woking.

Walter P. and Stoffers P. (1985) Chemical characteristics of metalliferous sediments from eight areas on the Galapagos Rift and East Pacific Rise between 2°N and 42°S. *Mar. Geol.* **65**, 271–287.

Young E. D., Galy A. and Nagahara H. (2002) Kinetic and equilibrium mass dependent isotope fractionation laws in nature and their geochemical and cosmochemical significance. *Geochim. Cosmochim. Acta* **66**, 1095–1104.

Ziegler C. L., Murray R. W., Hovan S. A. and Rea D. K. (2007) Resolving eolian, volcanogenic, and authigenic components in pelagic sediment from the Pacific Ocean. *Earth Planet. Sci. Lett.* **254**, 416–432.

Associate editor: Jérôme Gaillardet